POLITECNICO MILANO 1863

DIPARTIMENTO DI MECCANICA

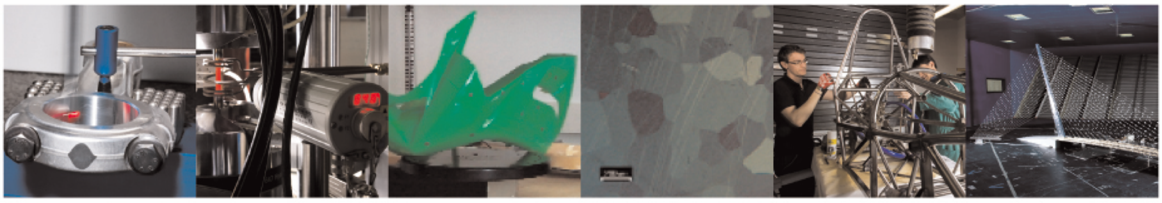

Sustainable 3D printing with recycled tire rubber-based filaments: an investigation of process parameters and mechanical behaviour

Badini, Silvia;Graziosi, Serena;Carboni, Michele;Regondi, Stefano;Pugliese, Raffaele

This is a post-peer-review, pre-copyedit version of Badini, S., Graziosi, S., Carboni, M., Regondi, S. and Pugliese, R. (2024), "Sustainable 3D printing with recycled tire rubber-based filaments: an investigation of process parameters and mechanical behaviour", Rapid Prototyping Journal, Vol. 30 No. 3, pp. 571-587. https://doi.org/10.1108/RPJ-08-2023-0309

DIPARTIMENTO DI MECCANICA ■ POLITECNICO DI MILANO
via G. La Masa, 1 ■ 20156 Milano ■ EMAIL (PEC): pecmecc@cert.polimi.it
http://www.mecc.polimi.it
Rev. 0

Rapid Prototyping J

Sustainable 3D printing with recycled tire rubber-based filaments: an investigation of process parameters and mechanical behaviour

Journal:	*Rapid Prototyping Journal*
Manuscript ID	RPJ-08-2023-0309.R1
Manuscript Type:	Original Article
Keywords:	sustainability, additive manufacturing, triply periodic minimal surface, sustainable development goals, recycling, waste tire rubber

Sustainable 3D printing with recycled tire rubber-based filaments: an investigation of process parameters and mechanical behaviour

Abstract

Purpose – This study evaluates the potential of utilising the material extrusion (MEX) process for recycling waste tire rubber. By investigating the process parameters, mechanical behaviour, and morphological characterisation of a thermoplastic polyurethane-waste tire rubber composite filament (TPU-WTR), the study seeks to establish a framework for end-of-life tire recycling using the MEX technology.

Design/Methodology/Approach – The research assesses the impact of various process parameters on the mechanical properties of the TPU-WTR filament. Hysteresis analysis and Poisson's ratio estimation are conducted to investigate the material's behaviour. Additionally, the compressive performance of diverse TPU-WTR triply periodic minimal surface lattices is explored to test the filament suitability for printing intricate structures.

Findings – Results demonstrate the potential of the TPU-WTR filament in developing sustainable structures. The MEX process can, therefore, contribute to the recycling of waste tire rubber. Mechanical testing has provided insights into the influence of process parameters on the material behaviour, while investigating various lattice structures has challenged the material's capabilities in printing complex topologies.

Social Implications – This research holds significant social implications addressing the growing environmental sustainability and waste management concerns. Developing 3D-printed sustainable structures using recycled materials reduces resource consumption and promotes responsible production practices for a more environmentally conscious society.

Originality – This study contributes to the field by showcasing the use of MEX technology for end-of-life tire recycling, particularly focusing on the TPU-WTR filament, presenting a novel approach to sustainable consumption and production aligned with the United Nations Sustainable Development Goal 12.

Keywords: sustainability, circular economy, recycling, waste tire rubber, additive manufacturing, triply periodic minimal surface, design for additive manufacturing, sustainable development goals.

Paper type: Research paper

1. Introduction

Tires are intricately designed products consisting of a carefully engineered combination of rubber, chemicals, carbon black, silica, fibreglass, and steel wire(Araujo-Morera *et al.*, 2021). About three-quarters of tiresare made of a rubbery compound(Amari *et al.*, 1999).

Tires play a vital role in enabling mobility and are fundamental to ensuring the safe operation of vehicles (Araujo-Morera *et al.*, 2021). They serve many essential functions, encompassing tasks like supporting the vehicle's weight and facilitating optimal grip for braking and acceleration on various surfaces. Nevertheless, managing end-of-life tires has become a significant global challenge due to the exponential growth in tire production each year(Nguyen *et al.*, 2022). Surprisingly, nearly 800 million tires are scrapped each year,and this data is projected to increase by around 2% each year (Sienkiewicz *et al.*, 2012). The automobile industry's continuous expansion has driven tire production to surpass a staggering 1.5 billion units per year (Toncheva *et al.*, 2021, Nguyen *et al.*, 2022).17 million tons of tires are estimated to be consumed on an annual basis(Alkadi *et al.*, 2019). To put this into perspective, the United States alone produces over 4 million tons of tires, while Europe produces 3.26 million tons, according to estimates by the International Rubber Study Group(Araujo-Morera *et al.*, 2021).

The expansive global market for tires generates a substantial annual demand for tire replacements, resulting in a significant accumulation of end-of-life tires (ELTs) that can no longer fulfil their intended function.The escalating volume of ELTs has led to pressing environmental concerns, primarily due to the intricate composition of tires, which poses significant challenges in managing their waste. Such tires exhibit exceptional resistance to both chemical and biological degradation, further complicating their proper disposal and recycling processes.Furthermore, resorting to landfilling as the primary method of disposing of used tires has various hazardous side effects. Discarded tires can serve as breeding grounds for mosquito larvae, which are carriers of life-threatening diseases like dengue, chikungunya, and malaria, owing to their ability to retain water (Nguyen *et al.*, 2022, Ramarad *et al.*, 2015, Zedler *et al.*, 2020). Additionally, when burned, tires contribute to substantial air pollution and can contaminate the soil, surface water, and groundwater, leading to various environmental issues (Worek *et al.*, 2022).

As underlined in(Nguyen *et al.*, 2022, Fazli and Rodrigue, 2020), there is an increasing inclination towards recycling waste tires into ground tire rubber(GTR) products. Nguyen and co-workers summarise significant advantages highlighted in the literature and related to the use of GTR-based fillers, which concern the possibility of reducing the costs of the final products and,in some cases,improving functionalities(Nguyen *et al.*, 2022).

Nowadays, the blending of GTR with various polymers, notably polypropylene (PP), polyethylene (PE), polyvinyl chloride (PVC) and polystyrene (PS) (Ramarad *et al.*, 2015, Jiang *et al.*, 2018, Liang *et al.*, 2020, Kosciuszko *et al.*, 2022), has opened up avenues for shaping and re-melting these materials into a diverse array of extruded and moulded products. Consequently, GTR blends have found practical applications in numerous aspects of everyday life, including running tracks and playground surfaces, to name a few(Toncheva *et al.*, 2021, Ferrao *et al.*, 2008).

Hence, the implementation of the circular economy (CE) model is gaining momentum within the tire industry. This shift stems from various factors, including the desire to explore new opportunities in the sustainable market, the necessity to comply with stringent environmental regulations, and the genuine conviction of companies that recognise the importance of minimising their ecological footprint. Embracing the CE approach allows tire companies to align with environmental objectives while tapping into the potential for long-term viability and positive environmental impact(Ramarad *et al.*, 2015).Due to this, recycling waste tires becomes an appealing choice for various potential applications. Among these, the Material Extrusion (MEX) process, and in particular,Fused Filament Fabrication (FFF),a well-established technology related to MEX, could offer several advantages of using sustainable and recycled feedstock materials(Ponis *et al.*, 2021, Schneevogt *et al.*, 2021, Fico *et al.*, 2022), such as recycled tire rubber. These materials could contribute to developing innovative and cost-effective topologically complex structures at different length scales for revolutionary applications,including materials science, civil engineering, scaffolding,and aerospace, to name a few.

FFF printers are readily available to a wider user base, from affordable desktop-size devices to large-scale industrial machines. This accessibility makes developing new materials for FFF easier, particularly focusing on waste and biomass by-products. As a result, scaling up these innovations in the mid-term becomes more feasible, opening up opportunities for the proliferation of novel applications (Romani *et al.*, 2023).

The role of the MEXprocess in promoting a more sustainable and circular economy is,therefore, already gaining momentum. For instance, the FFF technology has recently been employed to recycle various bio-based waste materials derived from industrial activities, like wood and timber waste (Filgueira *et al.*, 2018, Pringle *et al.*, 2018), herbaceous plants such as corn, rice, hemp, cork, cellulose (Biswas *et al.*, 2017, Coppola *et al.*, 1981, Gama *et al.*, 2021, Bahçegül *et al.*, 2020), as well as mussel and eggshell (Sauerwein and Doubrovski, 2018, Hega *et al.*, 2023). Bio-based waste and scraps are fillers in thermoplastic polymers like PLA, PP, CoPE, ABS, and TPU(Romani *et al.*, 2023).

Nevertheless, the framework of ELT in the Additive Manufacturing (AM)field is still in its infancy.Laoutid et al.(Laoutid *et al.*, 2021)reported the use ofdevulcanizedand vulcanised recycled tire rubber at different content (i.e., 15 and 30 %wt) as filler in thermoplastic polyolefin (TPO) and acrylonitrile butadiene styrene (ABS)polymer matrices to produce filaments suitable for FFF printing. However, both recycled tire-rubber-basedblends displayed a decrease in mechanical behaviours compared to the feedstock material. On the other hand, the recycled tire rubber blended with TPO showed a shape recovery of 97% after compression cycles.In (Wiśniewska *et al.*, 2023), polymer blends composed of GTR, ethylene-vinyl acetate (EVA) and carbon black (CB) at different concentrations are presented. That study demonstrates that these GTR-loaded polymer composites have promising characteristics concerning thermal stability, mechanical properties, electrical conductivity, and anti-flame properties. Its processability and printability potential have been mechanistically explained based on Melt Flow Rate (MFR) values. In (Khan and Faizan, 2023), the authors propose a novel material obtained by combining WTR and polypropylene (PP) at different concentrations. Results demonstrate that the presence of the WTR decreases the tensile strength of the composite compared to the virgin PP, but an increase in the elongation at break is observed. These results have been obtained by directly testing the fabricated filament. Alkadi et al.(Alkadi *et* *al.*, 2019)used 200-mesh GTR as a filler in a commercialised TangoPlus FullCure 930® (FLX930, Stratasys) polymer matrix to form composite ink for theircustom-made direct printing process.Toncheva et al.(Toncheva *et al.*, 2021) investigated recycled tire rubber powder's mechanical and thermal properties combined with a polyamide matrix. They used a Powder BedFusion (PBF) process, specifically the Select Laser Sintering (SLS) technology. The authors reported that the incorporation of recycled tire rubber negatively affects the degradation temperature, as well as the mechanical features. Such results guided the authors to limit the maximum loaded amount of tire to 30%wt.

This overview suggests that multiple AM processes can provideoperativemeans to support the introduction of ELT into the CE paradigmand that this is a growing field of research.Among the AM processes available, the MEX can play a key role in further boosting the research interests in this field. However, the processability and the design potential of 3D-printable filaments obtained by blending recycled tire rubber with a thermoplastic matrix have not yet been profoundlyinvestigated.Further insights on howto tune printing parameters to process this composite filament successfully are needed. Besides, the conditions that allow this composite to compete with its virgin condition regarding mechanical properties should be further understood. Also, how WTR-based composite filaments could be exploited in Design for Additive Manufacturing (DfAM) is equally fundamental to promoting its adoption in real applications.

This paper addresses all these aspectsbyinvestigatingthe printability, mechanical behaviour, and morphological characteristicsof a thermoplastic polyurethane-waste tire rubber composite filament (TPU-WTR 80/20 %wt). Concerning printability, this study explores the impact of various FFF process parameters: nozzle diameter, printing temperature, raster angles, extrusion multiplier, retraction distance, printing speed, fan speed, and wipe distance. Analysing these factors could providea comprehensive understanding of the TPU-WTR filament’s performance and optimal printing conditions.Besides, toassess the effect of WTR particles on the TPU matrix, the influence of these printing parameters on the mechanical behaviour of 3D-printed TPU-WTR samples is alsoexplored. Hysteresis analysis and Poisson's ratio estimation are also performed. Concerning DfAM, the possibility of exploiting this polymer blend for printing cellular structures has also been tested, specifically those generated from the followingTriply Periodic Minimal Surfaces (TPMSs): Gyroid, Schwartz Primitive, Honeycomb Gyroid, and Split-P. Their printability and mechanical behaviour in compression have been assessed.This is a further research contribution of thisstudy.

The interest in testing such structures also stems from their well-known outstanding properties that include the possibility to control their topological features mathematically, their highly interconnected porous architectures and high surface-area-to-volume ratio, as well as their tunable mechanical properties(Feng *et al.*, 2022). These features make them attractive for multidisciplinary biomedical, automotive, aerospace, chemical, and energy applications(Pugliese and Graziosi, 2023).Even seminal, these data could allow the engineering of well-defined and tailorable recycled tire rubber-based lattice structures, which can be used for multifunctional applications and further strengthen the interplay between AM and material researchas an important contributor to the CE paradigm.

Overall, the comprehensive investigation discussed in this study canextend the boundaries of the MEX process in the CE field and push forward the possibility of exploiting this waste tire rubber material for manufacturing complex structures for multidisciplinary applications. Besides, this work addresses the need to ensure sustainable consumption and production patterns, one of the United Nations Sustainable Development Goals (SDG 12).

2. Materials and Methods

This section first presents the two thermoplastic filaments analysed in this study: virgin TPU and composite TPU-WTR. Then, it outlines the printing technology and process parameters for manufacturingthe dogbone tensile specimens and TPMS-based lattice structures using those materials. Details about how these structures were designed are also provided. Finally, the mechanical testing phase is covered. It includes tensile tests for dogbone specimens, hysteresis analysis, Poisson's ratio measurement, and lattice compression tests. Details about the performed Scanning Electron Microscopy (SEM) and X-ray diffraction (XRD) characterisations are also provided.

2.1 Materials

Two thermoplastic filaments are considered in this study. The first is the standard Thermoplastic polyurethane (TPU) 80 Shore A with a 1.75 mm diameter (FlexMark8, Treed Filaments, Italy). It was used without further modificationsbecause it is the feedstock material for producing the TPU-WTR filament.Hence, the TPU filament represents the baseline. The second material is the TPU-WTR, specifically, Thermoplastic polyurethane (TPU)/micronized waste tire-rubber (WTR) (80/20 %wt) filament, 80 Shore A, with a 1.75 mm diameter (Pneumatique, Treed Filaments, Italy).

2.2Tensile specimens

The tensile specimens were designed according to the ASTM D638-14standard andthe dogbone type IV(Figure S1A). Considering the possible FFF-induced anisotropy, the effect of the printing direction (namely raster angles) and printing temperature was probed. Also, printing parameters were optimised(see Section 2.3) by evaluating their influence on the sample's mechanical properties.

Due to the unsuitablecross-section of type IV dogbones to perform a reliable Poisson's ratio estimation (see Section 2.4), for such tests, 7-mm-thick dogbones were designed according to ASTM D638-14 standard (type III). Size and geometries are provided in the Supporting Information (Figure S1B).

Type IV tensile specimens were printed considering three raster angles (0°, 90°, and 0°-90°, Figure S2) and three printing temperatures (220°C, 230°C, and 240°C). For each experiment, five samples were printed.

2.3 Lattices

The Functional Lattice Package (FLatt Pack) program (2021, University of Nottingham) (Maskery *et al.*, 2022) was utilised to generate Gyroid (G), Schwartz Primitive (P), Honeycomb Gyroid (HG), and Split-P (SP) TPMS-based structures. A unit cell size of 15 mm, with a 1 mm wall thickness, was adopted. 15 mm was the minimal printable dimension for the TPU-WTR filament printed with a 0.8 mm nozzle, leading to an acceptable lattice definition. Considering the nozzle diameter constraint and the different unit cell topologies, the chosen volume fractions (ρ') were 0.2 for G, 0.18 for S, 0.25 for HG, and 0.44 for SP (Figure 1).

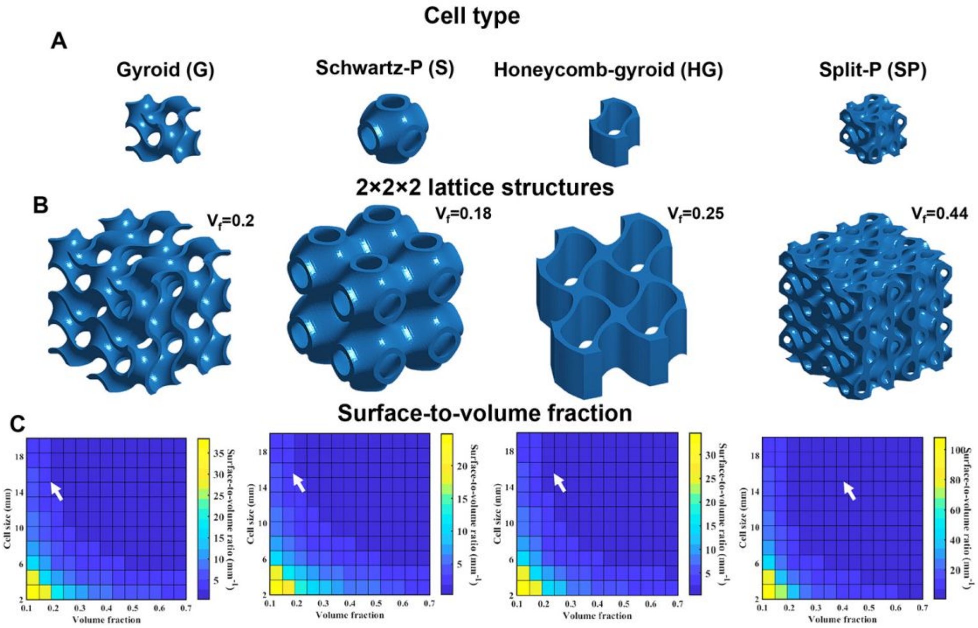

Figure 1. (A) Unit cell geometry of gyroid (G), schwartz-P (S), honeycomb-gyroid (HG), split-P (SP), and (B) corresponding to 2×2×2 lattice with different volume fraction (V_f). (C) The surface-to-volume ratio for each tested lattice was determined using the FLatt Pack "surface-to-volume estimation" feature.

Each lattice structure was designed as a linear repetition of two cells in each Cartesian direction, exported as ".stl" and sliced using the Simplify3D® software. The choice of geometry size was closely related to the 3D printer's capability to manufacture them accurately, which required proper tuning of the selected printing parameters (refer to Section 2.3). These 2×2×2 lattices were tested under compression.Besides, 4×4×4 arrays of Gyroid with volume fractions of 0.2 and 0.3 were considered suitable for estimating the relative lattice modulusthrough compression tests. This relative lattice modulus has been calculated as the ratio between the compression modulus of the lattice and Young's modulus of the bulk material(Maskery *et al.*, 2018a, Maskery *et al.*, 2018b, Ashby, 2005, Plocher and Panesar, 2020), and thus, through the following equation:

$$E' = \frac{E}{E_s} = C(\rho')^n \quad (1)$$

where E is the compression modulus of the lattice structure, E_s is the bulk Young's modulus of the material, and C and n are proportionality constants that depend on the lattice topology and the material used for manufacturing them and whose values can be retrieved experimentally, as in this study, or numerically(Ashby, 2006).

2.3 Printing technology and process parameters

The FFF Sharebot QXXL (Nibionno, Italy) was used to 3D-print all dogbones and TPMS structures. The printer has a maximum building volume of 700 × 350 × 300 mm^3 and operates at a layer resolution of 0.4-0.6 mm, using a nozzle with a diameter of 0.8 mm.The following printing parameters were kept constant: nozzle diameter (0.8 mm), infill (100%), and layer height (0.4 mm). The following parameters were tuned to probe the optimum printing combination: printing temperature, printing speed, wipe distance, fan speed, and retraction vertical lift (also known as "Z-hop").

2.4 Mechanical testing

*Tensile specimens.*Tensile tests under displacement control were conducted using an MTS Synergie 200 universal tensile testing machine equipped with a 1 kN load cell. The tests were conducted at a crosshead speed of 50 mm/min. Displacement measurements were taken using an MTS 632.26F-20 extensometer with a gauge length of 25 mm.

*Hysteresis specimens.*Tensile hysteresis tests were conducted to investigate the elastoplastic behaviours of the materials using an MTS Synergie 200 universal tensile testing machine equipped with a 1 kN load cell. The test focused on the effects of cycle number and strain amplitude. Loading and unloading were carried out with a constant crosshead speed of 50 mm/min, and each sample underwent 10 cycles at a maximum strain of 150%. The experiments were performed in triplicate to ensure accuracy and reliability.

*Poisson's ratio specimens.*Tensile tests under displacement control were conducted using an MTS Alliance RT/100 universal tensile testing machine equipped with a 100 kN load cell. The tests were performed with a crosshead speed of 2 mm/min, and the load was applied until it reached a maximum of 500 N. Two different experimental meanswere used for estimatingthe applied strain field: a bi-axial (tee) MM-F003109 strain gauge rosette and a video gauge ProViSys VideoTraction®. Reference points for video gauge were marked on samples using the mask from ProViSys supplied kit. The HBM Z70 cyanoacrylate adhesive was usedto bondthe strain gauge rosette. The calculation of the Poisson's ratio was performed as follows:

$$\nu = -\frac{\varepsilon_x}{\varepsilon_y} \qquad (2)$$

where ε_x is the transverse strain, taken as the negative lateral deformation in a specimen; $\varepsilon_y$is the axial strain, i.e., the positive longitudinal deformation.Each experiment was done in triplicate, and data were processed using Matlab™.

*Compression specimens.*Quasi-static compression tests were carried out on 2×2×2 lattices using the MTS Synergie 200 universal testing machine equipped with a 1 kN load cell. Each sample underwent three repetitions, and the tests were conducted at a crosshead speed of 5 mm/min, with a maximum crosshead displacement of 15 mm (equivalent to half of the sample height).

For the 4×4×4 lattices, the tests were performed using an MTS Alliance RF/150 machine. The testing was conducted with a crosshead speed of 15 mm/min, and the maximum crosshead displacement allowed was 30 mm (equivalent to half of the sample height).

The calculation of Young's modulus was performed as follows:

$$E_i = \frac{\sigma_i}{\varepsilon_i} \qquad (3)$$

where E is the Young's modulus in the direction i of interest; σ is the stress, calculated as the ratio between the reaction force and the area; ε is the strain, calculated as the ratio between the imposed displacement and initial length of the lattice in the *i*direction(Riccardo Sala *et al.*, 2022).

2.6 Scanning electron microscopy (SEM)

A characterisation of possible sagging, printing defects, and porosity of 3D-printed TPU-WTR specimens wasperformed using a SEM microscopy (Zeiss EVO 50) operating at 30 kV. All samples were sputter-coated with 4 nm of gold before the test.

2.7 X-ray diffraction (XRD)

A Rigaku SmartLab SE diffractometer in *q*-*q* configuration was employed to obtain the diffraction patterns of TPU and TPU-WTR materials. Diffracted beam was detected from 5 to 80 °2*q*, with a scan rate of 2°/min and a step size of 0.02°, through a 1D D/teX Ultra 250 detector.

3. Results and Discussion

This Section starts by providing the results concerning the printability of the TPU-WTR filament and continues by explaining how printing parameters influence the material's tensile properties. Open issues concerning filament production are discussed. Then, the Section details the results obtained concerning hysteresis characterisation, Poisson's ratio assessment, printability and mechanical performance in compression of TPMS-based lattices printed with the TPU-WTR-filament.

3.1 Printability of recycled tire rubber-based filament

This section focuses on the optimal printing parameters for manufacturing TPU-WTR-based filament compared to virgin TPU. This investigation is significant as the properties of TPU-WTR differ from those of virgin TPU due to the presence of waste tire rubber (WTR) particles. Therefore, identifying the optimal printing parameters for TPU-WTR is crucial to achieving the desired printing quality and functionality that can serve as a reference for researchers and industry professionals interested in using TPU-WTR-based filaments in their manufacturing processes.

The printing parameters for TPU were established based on previously reported research(Sala *et al.*, 2022), while those for TPU-WTR were fine-tunedhere using the TPU parameters as a starting point. For clarity, all optimised printing parameters are provided in Table S1.

A 0.8 mm nozzle diameter was used to prevent clogging caused by the accumulation of WTR particles in the extruder. The layer height was fixed at 0.4 mm, and retraction was avoided due to the soft nature of both materials, as previously reported(Sala *et al.*, 2022). The optimal printing speed was 1,000 mm/min to prevent overheating or hindered extrusion.

To ensure homogeneous infill, several parameters were tested and tuned. Firstly, the extrusion width was increased from 0.90 to 0.96 mm to avoid under-extrusion issues, which could result in voids in the printed sample.Additionally, to prevent stringing, a wipe distance of 5 mm and an extra restart distance of 2 mm were implemented every time the nozzle performed a free movement. The outline overlap was 70% to prevent under-extrusion and avoid overheating issues. Furthermore, the outline under-speed was fixed at 75%, reducing the printing speed of the perimeter by about 25% to allow for more precise deposition of the material and a sharper definition of the specimens' edges. A 2.5 mm coasting distance and 1 mm of retraction vertical lift were selected to prevent the formation of material drops during layer deposition. Lastly, a build platform temperature of 60°C was chosen to increase the specimens' adhesion. At the same time, the fan speed was fixed at 20% from the second layer to enhance the uniformity and printing quality of the object.

Upon a preliminary visual inspection, the fine-tuned printing parameters resulted in satisfactory sampleprinting with the three different raster angles (Figure 2A), especially considering the recycled nature of the filament. Nevertheless, in the sample printed at 220°C and 240°C, noticeable voids in the upper surface, sidewalls, and other imperfections of the layers are observable after the manufacturing process (Figure 2B). These voids might lead to an impairment of mechanical behaviour, which will be considered in Section 3.2. Instead, when examining the upper surface and sidewalls of samples printed at 230°C, a uniform and debris-free filling is evident, with no stringing, voids, or excessive filament lumps. Nevertheless, this approach ensured that the parameters were tailored to the unique properties of TPU-WTR and led to successful printing outcomes. By adjusting the parameters, challenges were overcome, such as clogging of the nozzle due to the accumulation of WTR particles and the soft nature of TPU-WTR, which can lead to under-extrusion and overheating. The optimisationof printing parameters is crucial for achieving the desired printing quality and functionality of such recycled filaments.

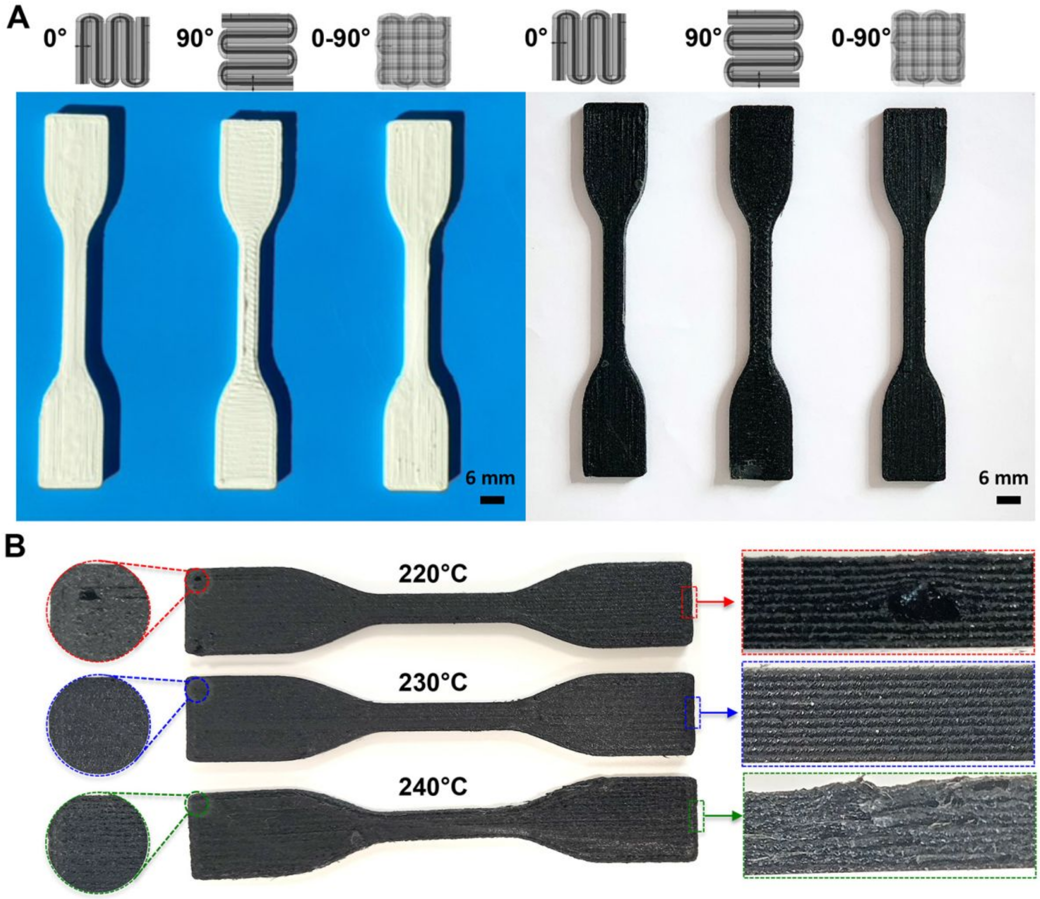

Figure 2. (A) ASTM D638-14 type IV dogbone specimens of TPU (on the left) and TPU-WTR (on the right) printed at three different raster angles (0°, 90°, 0°-90°). (B) Detailed comparison of printing quality achieved with the three nozzle temperatures of 220°C, 230°C, and 240°C. The sample printed at 230°C shows high quality and definition without any visible defects, whereas samples printed at 220°C and 240°C exhibit holes, voids, and overheating issues, indicating a lack of material homogeneity and decreased interlayer adhesion.

3.2 Effect of printing directions and printing temperature on the tensile modulus

Displacement-controlled tensile tests were conducted to gain insights into the mechanical behaviour of each type IV dogbone specimen, following the ASTM D638-14 standard(see Materials and Methods for further details). The experimental tensile tests showed no effect of the raster angles (0°, 90°, and 0°-90°) and printing temperature (220°C, 230°C, and 240°C) *vs.* loading direction for both TPU (Figure 3A) and TPU-WTR (Figure 3B) samples.

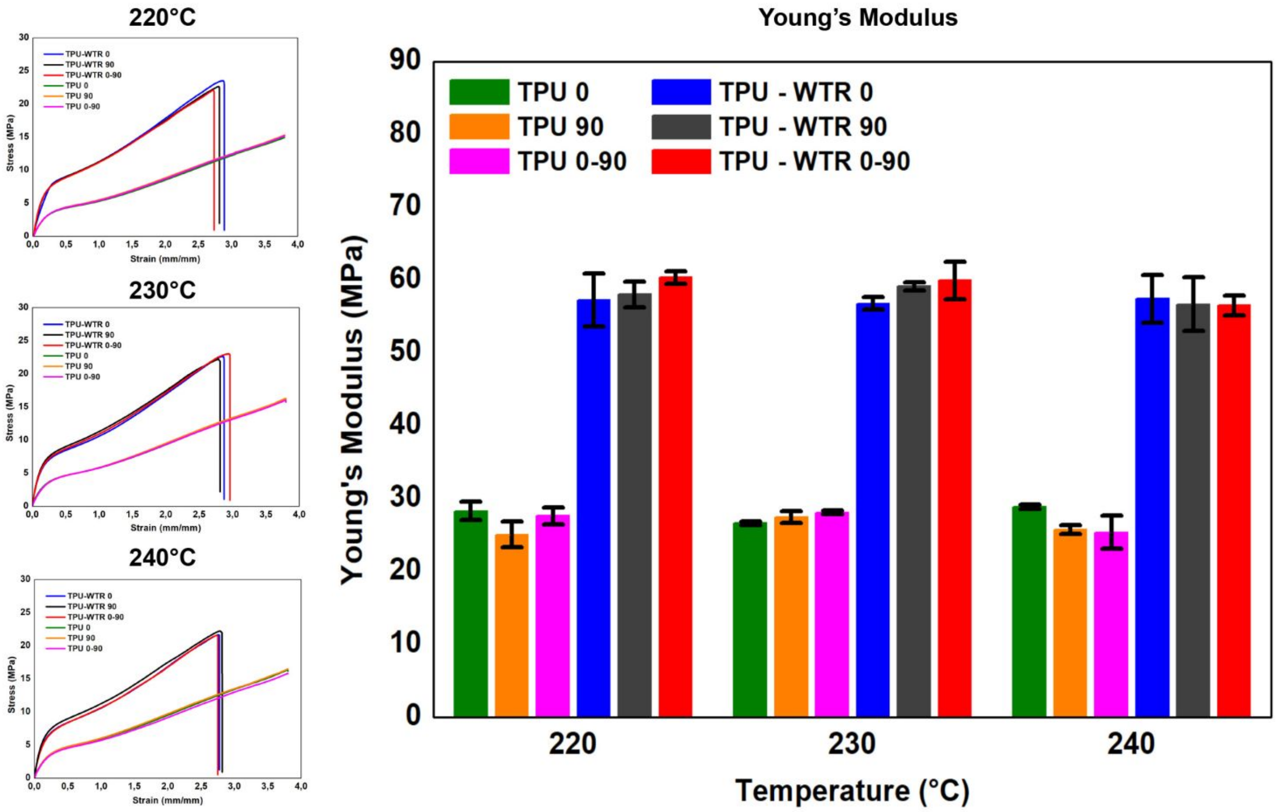

Figure 3. Effect of raster angles (0°, 90°, and 0°-90°) and printing temperature (220°C, 230°C, and 240°C) under tensile loading for TPU and TPU-WTR samples. All samples showed an isotropic-like mechanical behaviour along printing directions. However, recycled tire particles in TPU-WTR significantly increased its tensile behaviour compared to wild-type TPU.

The ANOVA analysis further corroborated this observation. Additionally, it was observed that all samples exhibited similar isotropic-like mechanical behaviour along *x* (i.e., raster angle of 0°) and *y* (i.e., raster angle of 90°) printing directions. However, recycled tire particles in the TPU-WTR materials significantly enhanced its tensile behaviour. The average TPU-WTRYoung's modulus is 58 ± 2.05 MPa, compared to the wild-type TPU with an average Young's modulus of 27 ± 0.96

MPa. For clarity, the mean values of Young's modulus referred to each sample with different raster angles and printing temperatures are provided in Table I.

	Raster angle	Temperature (°C)		
		220	230	240
E_{TPU} (MPa)	0°	28.30 ± 1.30	26.63 ± 1.74	28.87 ± 1.17
	90°	25.07 ± 0.25	26.63 ± 1.74	25.73 ± 0.25
	0°-90°	27.60 ± 0.27	28.10 ± 0.61	25.37 ± 2.25
$E_{TPU\text{-}WTR}$ (MPa)	0°	57.23 ± 3.62	56.76 ± 0.85	57.44 ± 3.27
	90°	58.02 ± 1.78	59.13 ± 0.59	56.70 ± 3.68
	0°-90°	60.37 ± 0.88	59.96 ± 2.59	56.50 ± 1.37

Table I. Comparison of average values of Young's modulus of TPU and TPU-WTR with different raster angles of 0°,90°, 0°-90° and printing temperatures of 220°C, 230°C, and 240°C.

This finding contrasts with those reported by Laoutid et al.,(Laoutid *et al.*, 2021) which showed that the inclusion of recycled tire particles in the TPU matrix reduces Young's modulus, thereby weakening the overall mechanical behavior.This discrepancy in the results could be attributed to various factors, such asa difference in the mixing process of the tire particles with the TPU matrix andthe fact thatthe TPU filament used as the matrix and the one containing tire particles have different Shore values(Laoutid *et al.*, 2021). Indeed, it is essential to note that in the present study, both filaments (i.e., the virgin TPU and the TPU-WTR) have the same Shore value of 80A(see Section 2.1). In addition, the TPU-WTR filament comprises 56% tire rubber particles ranging in size from 0.121 to 0.257 mm, with 2.34% of particles having a 0.3 mm diameter (see Figure S5 for data provided by the supplier).

Also, TPU-WTR samples demonstrated an average strain at failure of 263 ± 19.49%, while the wild-type TPU did not break. This indicates that the stiffest TPU-WTR material is more brittle and has lower elongation thanthe virgin TPU. The fact that all TPU-WTR dogbone samples failed enabled the analysis of peak stress and elongation at break (as shown in Figure S3). These data confirmed the previously stated isotropic-like behaviourbecause the values of these properties are similar despite the different raster angles and printing temperatures. This information, never reported in the literature for what the authors know, provides relevantinsights into the material's performance under stress.

Overall, the findings suggest that the inclusion of recycled tire particles in a TPU matrix can significantly impact the mechanical behaviour of the resulting filament, depending on various factors such as the mixing process and the Shore value of the materials used. Furthermore, the consistent mechanical properties in all tested raster angles and printing temperatures indicate that the material is reliable and can withstand stress from any direction.

Lastly, since the tensile behaviour of both material samples was unaffected by printing temperatures and directions, the “best-performing sample” selection for the remaining tests of the study was based on printing quality (as described in Section 3.1). Figure 3B illustrates that dogbones printed at 220°C and 240°C exhibited voids and poor interlayer adhesion, whereas those printed at 230°C showed good adhesion and high definition. Moreover, dogbone specimens printed with raster angles of 90° and 0°-90° displayed a higher incidence of printing defects compared to those printed at raster angle of 0°. Based on these findings, the dogbone printed at 230°C with a raster angle of 0° was identified as the "best-performingsample".

3.3 Open issues related to the tire-elastomer compound filament production

Thepotential issues concerning the manufacturability of tire-elastomer compoundsas 3D-printable filaments were also investigated. This is essential as negative implications may arise, which can compromise the printability and mechanical behaviour of the materials. While these issues are typically associated with industrial manufacturing of recycled raw materials, they have significant implications for researchers looking to apply them,thanks to AM,for real-world applications. Therefore, it is essential for researchers to carefully consider the compatibility of the tire-elastomer compound when using recycled raw materials to ensure optimal printability and mechanical behaviour of the resulting materials.

Incorrect compound formation or improper storage procedures during filament manufacturing can result in difficulties during printing and suboptimal performance for the final printed object. By using scanning electron microscopy (SEM) analysis, in this study, the differences between an incorrect tire-elastomer compound used to produce the filament (namely spool 1) and a properly casted filament (namely spool 2) were analysed.

When using an incorrect tire-elastomer compound, the final printed object may exhibit a poor appearance, including cracks, high porosity, low homogeneity within the same printing pass, and poor interlayer adhesion (Figure 4A and Figure S4). In contrast, a properly casted filament(i.e., the spool 2) provides a high-quality printed object (Figure 4B) with no visible defects, lumps, or strings.

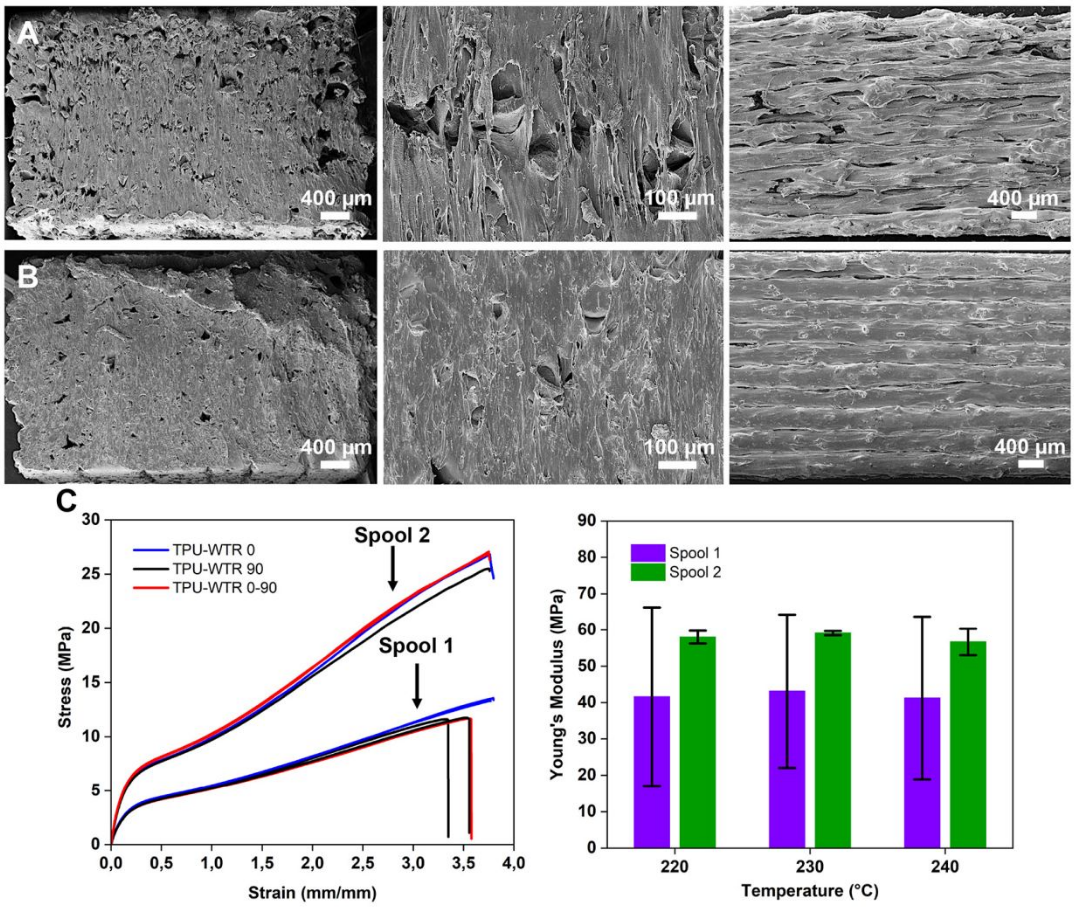

Figure 4. SEM analysis of (A) TPU-WTR dogbone made from an incorrect tire-elastomer compound and (B) adequately casted TPU-WTR filament. The incorrect compound formation resulted in poor appearance and low interlayer adhesion of the final printed dogbone, while the properly casted filament provided a high-quality printed dogbone with no visible defects. (C) Comparison between the Young's Modula obtained with dogbones printed with an incorrect (spool 1, in purple) and a correct (spool 2, in green) TPU-WTR compound under tensile loading.

In addition, incorrect polymer mixing may lead to poor mechanical properties, resulting in low printing predictability and preventing reproducibility (Figure 4C). Indeed, spool 2 displayed higher Young's Modulus values (similar to those obtained in Section 3.2) and lower standard deviation.

Thus, it is critical to use proper compound formation and storage procedures during filament manufacturing to ensure optimal printing and mechanical performance of the final object.

A preliminary analysis was conducted to understand the significant difference in behaviour between the two filaments. As mentioned above, the TPU-WTR filament comprises 56% tire rubber particles ranging in size from 0.121 to 0.257 mm, with 2.34% of particles having a 0.3 mm diameter (see Figure S5 for data provided by the supplier). This wide range of particle sizes creates inherent material issues during FFF. The larger particles tend to accumulate at the end of the nozzle, obstructing the path and quickly clogging the nozzle when a 0.4 mm diameter nozzle is used. Additionally, it is physically impossible to achieve a homogeneous layer height below 0.3 mm.

The limitations caused by this intrinsic issue and incorrect mixing are the primary reasons for the vast differences between the two spools. The behaviour and appearance of spool 1 can be due to an inadequate homogenisation of tire rubber particles in the TPU matrix during the compounding phase. As a result, the incorrectly mixed filament has low interfacial adhesion between components, resulting in worse mechanical properties than the other filament. Incorrect mixing renders the performances of TPU-WTR filament comparable to those of virgin TPU, eliminating its potential as an alternative to standard TPU. The partially recycled nature of TPU-WTR material becomes worthless, losing its added values related to sustainability. In addition, the inability to achieve consistent and predictable mechanical properties due to incorrect mixing makes it impossible to benefit from the strengths of AM. Hence, if incorrectly mixed filament standardisation cannot be achieved, TPU-WTR becomes industrially useless even with alternative production techniques. Thus, to stick to CE principles, recycled materials must not only be recycled, but they must also bring improvements to the existing settings.

3.4 Hysteresis characterisation

This section discusses the hysteresischaracterisation performed to determine any differences in the stabilisationbetween TPU and TPU-WTR materials. As shown in Figure 5, the analysis revealed that TPU-WTR exhibited more plastic behaviourthan TPU, with a residual strain of 43.72 ± 0.34% and 28.73 ± 1.15% after the first cycle, respectively. As expected, wild-type TPU demonstrated superior elastic behaviour with higher elastic recovery and a lower hysteresis area, indicating lower energy loss. After stabilisation (starting from the 6th cycle), the difference in loss of elasticity between the two materials suggested that TPU recovered 14.8 ± 0.14% more strain than TPU-WTR. However, the stabilisedhysteresis loop sizeremained nearly unchanged for both materials, indicating the absence of additional relevant rearrangementof the polymeric chains network. While TPU recovered a higher percentage of strain along the same loading history, the loss of elasticity had the same impact on both materials, as evidenced by the increase in residual strain between the first and last cycle (14.98% for TPU and 14.78% for TPU-WTR). Detailed data of residual strain after the 1st and 10th cycle of hysteresis are reported in Table S2.

TPU is a pure soft elastomer with high elasticity and a fast elastic return, resulting in low stiffness. In contrast, the presence of waste tire particles in TPU-WTR improves its mechanical properties but also enlarges the hysteresis area and intrinsically decreases elasticity, thus showing a wider gap between each set point at the end of each cycle compared to TPU and, accordingly, a higher amount of energy loss and a slower return to its equilibrium condition.

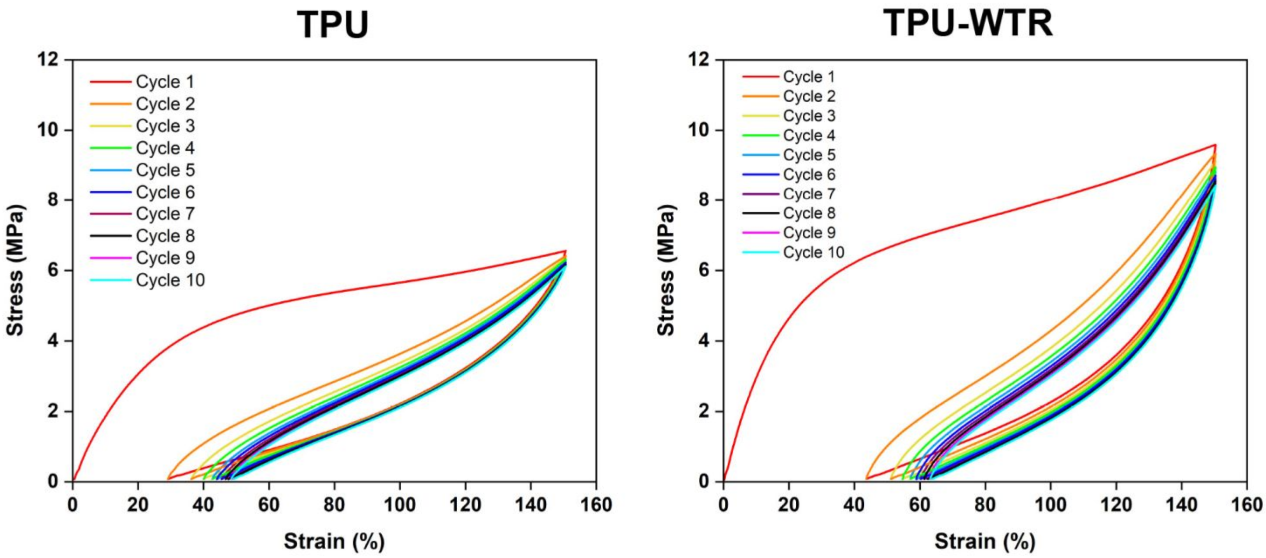

Figure 5. Hysteresis curves with mean values ofTPU and TPU-WTR samples.

3.5 Poisson's ratio assessment

To provide a comprehensive characterization of the TPU-WTR material, Poisson's ratio (ν) estimation was assessed using the "best-performing sample" (dogbone printed at 230°C with a raster angle of 0°, Section 3.2). Due to the inherent difficulties in testing and assessing axial (ε_y) and transverse (ε_x) strain for FFF-printed materials, two different gauges were employed. The strain was measured with a bi-axial strain gauge MM-F003109 in combination with a video gauge ProViSys VideoTraction, as shown in Figure 6A (see Section 2.4 for further details).

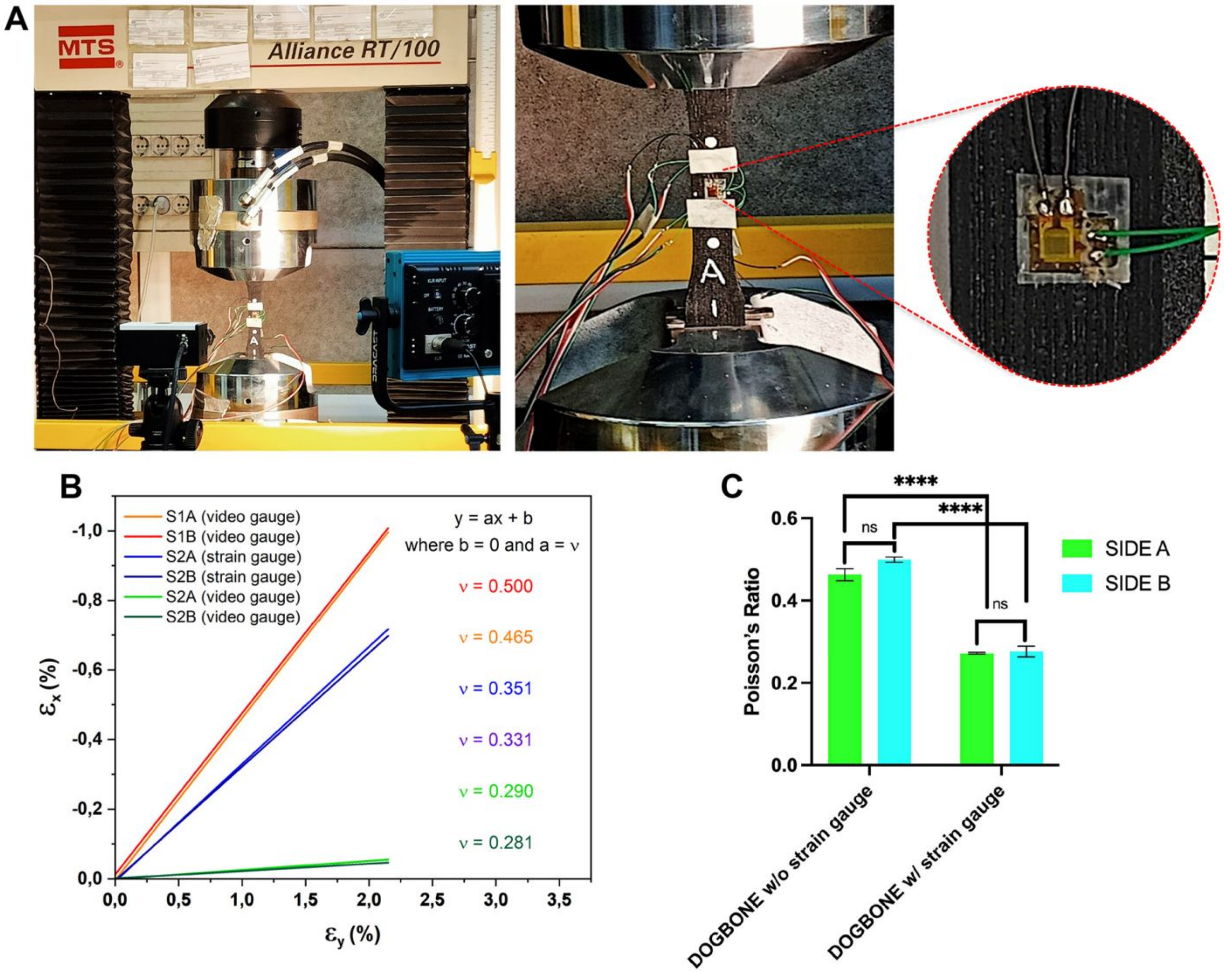

Figure 6. (A) The testing set-up for the Poisson's ratioassessment showing a bi-axial strain gauge MM-F003109 in combination with a video gauges ProViSys VideoTraction. On the right, the magnification of ASTM D638-14 dogbone type III shows the strain gauge connected to the sample by cyanoacrylate adhesive.(B) Graph of $\varepsilon_y vs. \varepsilon_x$ of tested TPU-WTR samples. The slope of each curve identifies Poisson's ratios. S1 and S2 stand for sample 1 and sample 2, respectively, while letters A and B define the dogbone's bottom and top layers. (C) Statistical analysis on the Poisson's ratio of the samples with and without strain gauges. There is no statistically significant difference between the two sides of the same sample (labelled with *ns* = "not-significant"). Instead, a statistically significant difference ($^{****}p<0.0001$) between the same faces of the two considered samples was found, ascribable to the cyanoacrylate adhesiveused for strain gauge installation, which affects the test locally along the x direction, thus increasing the sample's stiffness and reducing Poisson's ratio.

Figure 6B displays the ε_x and ε_y data; their slopes correspond to the ν values. The first sample (S1) was tested with the video gauge only, while the second sample (S2) was tested using strain gauges in combination with a video gauge. Since the FFF technology exhibits different finishing between the first and the last deposited layer, both sides of the samples were used to obtain the Poisson's value experimentally. In the graph of Figure 6B, sides labelled with "A" are those representing the bottom layer (i.e., the firstprinted layer),while those markedwith "B" represent the top layer (i.e., the last layer printed). The results showed a clear difference in behaviour between the sample with and without strain gauges. For sample S1, the average value of Poisson's ratio from video gauge data was $\nu = 0.482 \pm 0.025$. The ν values of sides A and B were 0.500 (in red) and 0.465 (in orange), respectively. These values are close enough to state that the different surface irregularities caused by the FFF process do not affect Poisson's ratio.

Instead, for sample S2, the average Poisson's ratio from video gauge data was $\nu = 0.286 \pm 0.006$, while from strain gauges data, is $\nu = 0.341 \pm 0.014$. Again, strains from different sides are similar, thus confirming the previous statement. The ν values of sides A and B were respectively 0.290 (in light green) and 0.281 (in green) for video gauge and 0.351(in blue) and 0.331 (in purple) for strain gauges.However, the change in Poisson's ratio between the two samples could be caused by thecyanoacrylate adhesive used to connect strain gauges to sample S2, as described in Section 2.4. The FFF technology intrinsically brings micro-voids between layers, and the cyanoacrylate adhesive can fill such micro-voids, stiffening the entire area and providing lower strain values. In particular, we noticed that ε_x was affected by the presence of the cyanoacrylate adhesive, while all ε_y values are comparable between the two dogbones (Table II). This could potentially be associated with the printing direction of the tested dogbones, specifically the 0° raster angle. It could be claimed that if a 90° raster angle had been considered, this variation would have been flipped, affecting the longitudinal strain ε_y and not the transverse one. To support such insights, recently published studies reported the effect of oriented voids linked to the printing direction in FFF samples (Sigmund A. Tronvoll *et al.*, 2018, Jafar Ghorbani *et al.*, 2022, Yubo Tao *et al.*, 2021, Wang *et al.*, 2022). In addition, another potential issue with utilizing bi-axial strain gauges arises when the stiffness of the polymeric material composing the strain gauge support closely resembles that of the 3D printed material. In such cases, the strain gauge becomes actively involved in influencing the test, thereby stiffening the entire area and yielding lower strain values.

S1A (video gauge)		**S2A (video gauge)**		**S2A (strain gauge)**	
εx (%)	**εy (%)**	**εx (%)**	**εy (%)**	**εx (%)**	**εy (%)**
- 0.2	0.45	- 0.11	0.41	- 0.1	0.31

S1B (video gauge)		S2B (video gauge)		S2B (strain gauge)	
εx (%)	εy (%)	εx (%)	εy (%)	εx (%)	εy (%)
- 0.19	0.38	- 0.1	0.38	- 0.14	0.36

Table II. Values of ε_x andε_y at the reference stress of 0.3 MPa, showing that ε_x was affected by the presence of the cyanoacrylate adhesive while all ε_y values are comparable between the two samples, S1 and S2 with and without strain gauge.

Lastly, Figure 6C shows the statistical analysis of Poisson's ratio of the two samples. As expected, there is no statistically significant difference between the two sides of the same sample, thus supporting the non-dependency of Poisson's ratio on the printing side in FFF samples. On the contrary, a statistically significant difference ($^{****}p<0.0001$) between the same faces of the two considered samples was found.

To summarise, the use of video gauge is more reliable to estimate the Poisson's ratio of 3D-printed TPU-WTR material (and in general for 3D-printed soft polymers) compared to strain gauges where the presence of cyanoacrylate adhesive in micro-voids negatively affects the accuracy of the analysis. Additionally, the obtained Poisson's ratio from the video gauge of 0.482 ± 0.025 is consistent with the Poisson's ratio of compound rubber-tire, which is 0.49 (Simon and Bárány, 2023). These preliminary findings could be valuable for expanding research on TPU-WTR performance, particularly in predicting its behaviour in specific fields of interest through computational studies such as Finite Element Analysis (FEA).Furthermore, such a methodology that combines a bi-axial strain gauge with a video gauge provides a dual benefit. Firstly, it offers valuable insights for estimating Poisson's ratio in the context of FFF technology. Notably, the methodology reveals that although FFF technology presents different finishes between the first and last layers deposited, this does not impact Poisson's ratio. Secondly, this methodology highlights that since FFF technology inherently generates micro-voids between layers, using strain gauge cyanoacrylate adhesive can negatively affect Poisson's ratio, as it stiffens the entire area and produces lower strain values. Consequently, the obtained results suggest that video gauge results are more reliable for 3D-printed polymer testing. These findings are particularly relevant for researchers working with FFF technologies and polymers.

3.6 X-ray diffraction analysis

X-ray diffraction (XRD) analysis was conducted on TPU and TPU-WTR filaments to elucidate their crystalline structures (Figure 7). The XRD pattern of the TPU sample revealed a broad reflection at 2θ of 20.04°, indicative of its amorphous nature. However, distinctive small, sharp crystalline reflections at 2θ values of 27.48°, 36.14°, and 54.22° were observed, suggesting the presence of long-range crystalline hard segments intermingled with the soft blocks(Lu Liu *et al.*, 2017).

In contrast, the TPU-WTR samples exhibited amorphous structures, as evidenced by a broad reflection at 2θ of 20.72°. This characteristic reflection was attributed to the presence of natural rubber and styrene-butadiene rubber in the TPU-WTR formulation(Gonzalo Martínez-Barrera *et al.*, 2020).

These findings underscore the diverse crystalline compositions and arrangements within TPU and TPU-WTR, shedding light on the nuanced structural characteristics of these materials. Such insights are useful for better understanding their mechanicalproperties, thereby informing potential applications in various industrial contexts.

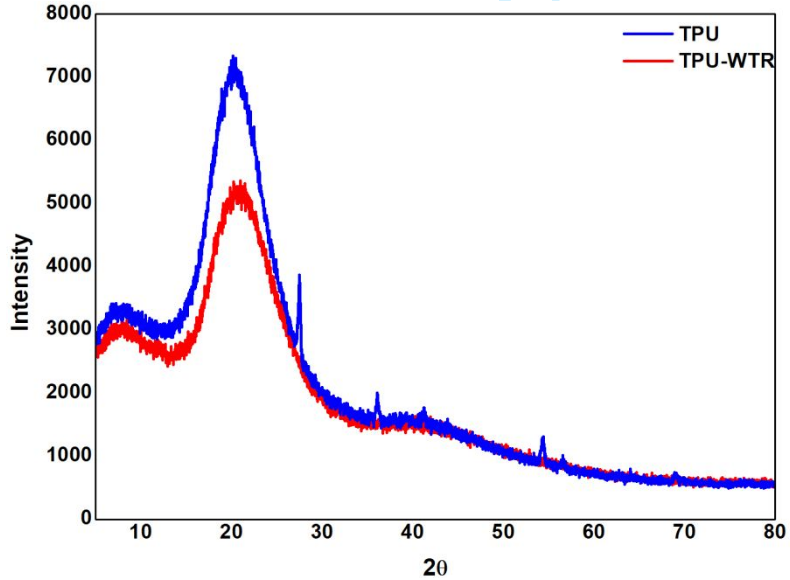

Figure 7. The XRD patterns of the TPU (blue line) and TPU-WTR (red line) to discrete reflections at appropriate 2θ values.

3.7 Printability and mechanical performance of tire rubber-based TPMS structures

As a proof of concept, we evaluated how the recycled TPU-WTR filament influences the performance of various TPMS structures. The Gyroid (G), Schwartz-P (S), Honeycomb-gyroid (HG), and Split-P (SP) unit cells were generated as periodic matrices and then converted into three-dimensional cuboid structures, as previously reported (Sala *et al.*, 2022).

We optimized printing parameters for each TPMS structure to ensure high printing quality (Table S3). In particular, the extrusion multiplier was brought from 1 to 1.1, and a printing temperature of 220°C was employed compared to the 230°C used for manufacturing the best-performing tensile specimens to avoid debris and lumps of filaments. The printing speed was 1,500 mm/min with a 50% speed reduction for better layer deposition. Retraction between layers was turned off to prevent stringing and nozzle clogging, and a 2 mm coating and extra restart distances were set to avoid over-deposition of material.

After an initial visual inspection, it was observed that the tuned process parameters yielded satisfactory results regarding the printing quality of the samples. This was especially impressive given the filament's recycled and flexible nature and the printed structures' complexity, as shown in Figure 8 A-D.

Upon closer examination of the lattice structures' surfaces, it was noted that the filling was uniform, with no debris or stringing inside the structures. Furthermore, after manufacturing, there were no visible voids in the sidewalls or other imperfections or irregularities of the layers. The SEM analyses (Figure 8 A-D) confirmed these findings, as none of the 3D-printed TPMS structures exhibited defects such as sagging, improper layer adhesion, or porosity. Also, tire rubber micro-particles of varying sizes were observed at higher magnifications in the SEM images.

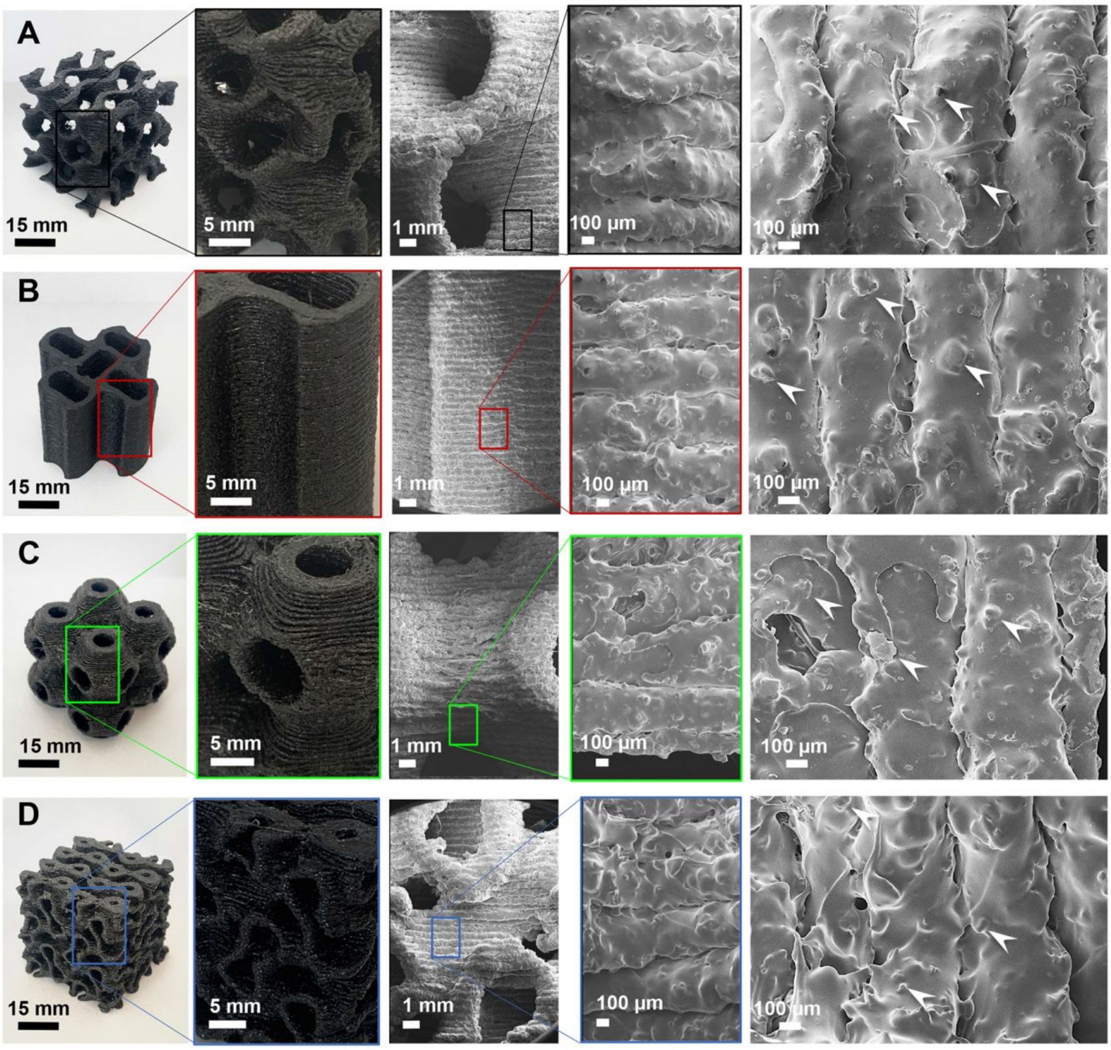

Figure 8. SEM images of the TPU-WTR-based lattice structures: (A) Gyroid, (B) Schwartz-P, (C) Honeycomb-gyroid, and (D) Split-P. The magnification of the surface (in black, red, light green, and blue) shows the printing quality of all recycled lattices. In the magnification on the right, the arrows indicate tire rubber micro-particles.

Next, the compressive behaviour of all 3D-printed structures was examined (Figure 9A-C). It is important to note that the obtained data cannot be strictly compared due to the different relative densities of the lattice structures. However, it is possible to evaluate them by considering that all structures were printed at the minimum possible volume fraction with the current FFF limitations for the TPU-WTR. All TPMS samples with different volume fractions exhibited qualitatively similar stress-strain responses, as shown in Figure 8A. Howdensification occurs after reaching the peak stress varies depending on the cell topology, as demonstrated in Figure 8B for the SP, G, P, and HG structures during compressive tests.

The Young's moduli of all TPMS structures were extracted from the stress-strain response and calculated using Eq. (3). Figure 8C shows the average Young's modulus for all tested cell topologies. Specifically, the SP structure displayed Young's modulus of 3.23 ± 0.001 MPa, followed by G with a modulus of 2.05 ± 0.59 MPa. Despite having the lowest volume fraction, P had Young's modulus of 1.33 ± 0.37 MPa. Lastly, the honeycomb-gyroid structure (HG) exhibited Young's modulus of 0.80 ± 0.20 MPa.

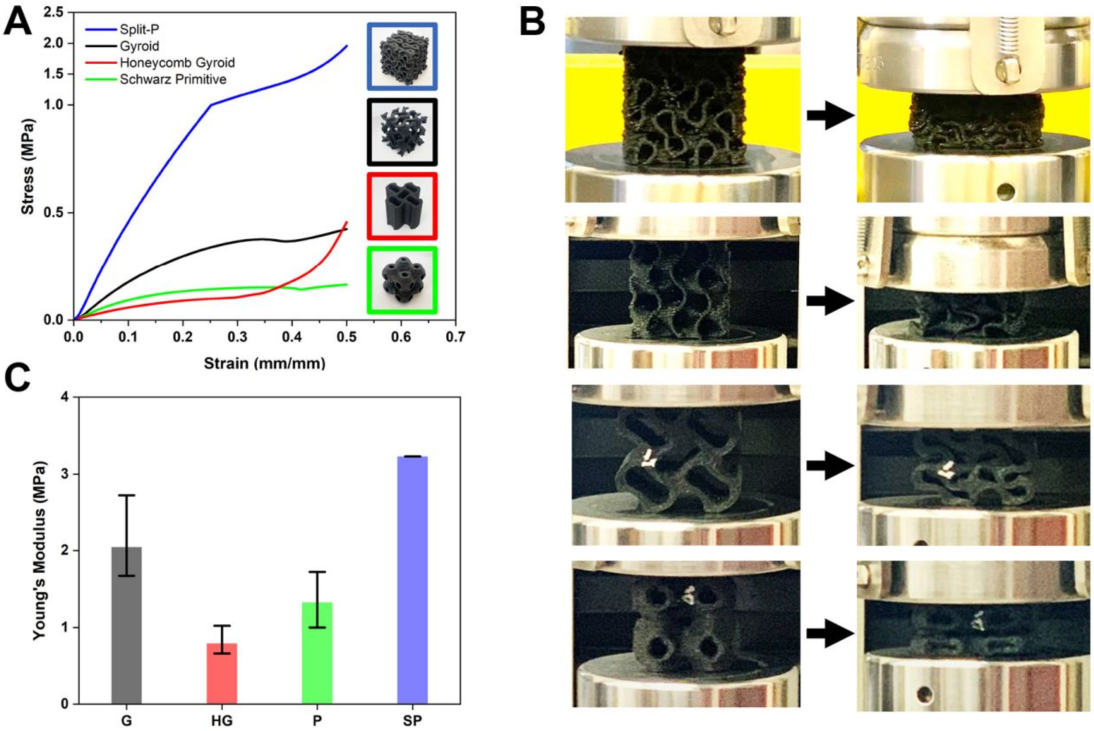

Figure 9. Quasi-static compression tests of 3D-printed TPMS structures. (A) The stress-strain response of TPMS samples. (B) SP, G, P, and HG densification after peak stress. (C) Average Young's modulus of all tested cell topologies, with SP having the highest modulus and HG having the lowest. Note that the obtained data cannot be strictly compared due to the different relative densities of the lattice structures.

The elastic modulus of TPMS structures increases steadily as the number of unit cells rises, eventually reaching a maximum limit. This gradual enhancement in elastic modulus can be ascribed to the reduced impact of cells with exposed surfaces on the overall rigidity of the TPMS structure. Consequently, a more precise depiction of cell deformation emerges, resembling that of a homogeneous porous solid. Maskery et al., (Maskery *et al.*, 2018b) found that the arrangement of 4 × 4 × 4 lattices achieves an elastic modulus of only 0.2% below the upper bound, making it a sensible approximation for the elastic modulus of the lattice structure, as though it were a homogeneous porous solid. Given the fundamental significance of this aspect, 4 × 4 × 4 gyroid lattices made of TPU-WTR with the same cell size (15 mm) and two different volume fractions (0.2 and 0.3) were printed and tested. The gyroid lattice, widely employed in various application fields, from energy to biomedical (Downing *et al.*, 2021, Monkova *et al.*, 2017, Yan *et al.*, 2015), was chosen as the blueprint for TPMS structures.

Figure 10A presents the average stress-strain compression curves for gyroid samples with volume fractions of 0.2 (blue) and 0.3 (red). The average Young's modulus for the volume fractions of 0.2 and 0.3 are 5.57 ± 0.04 MPa and 6.11 ± 0.09 MPa, respectively. Both samples exhibited a decrease in elasticity after the initial loading-unloading cycle, with the gyroid lattice at a volume fraction of 0.2 experiencing a 7% reduction. The gyroid structures with higher relative density exhibited a 7.5% reduction. Furthermore, the peak stresses at 50% strain were measured at 0.81 ± 0.01 MPa and 1.03 ± 0.02 MPa, respectively.The influence of relative density on the overall mechanical behaviourof 4 × 4 × 4 gyroid arrays is illustrated in Figure 10B. A straight interpolation line was calculated by plotting the relative compressive modulus (E') of 4 × 4 × 4 gyroid arrays with volume fractions of 0.2 and 0.3 against their relative density (ρ’). This relationship, $E' = C(\rho')^n$, was determined for TPU-WTR gyroid arrays, where C = 0.3569 and n = 1.12. The obtained power trend aligns well with the one attributed to stretch-dominated structures, such as the gyroid, where the exponential value is typically around 1 (DeValk and Lakes, 2021).

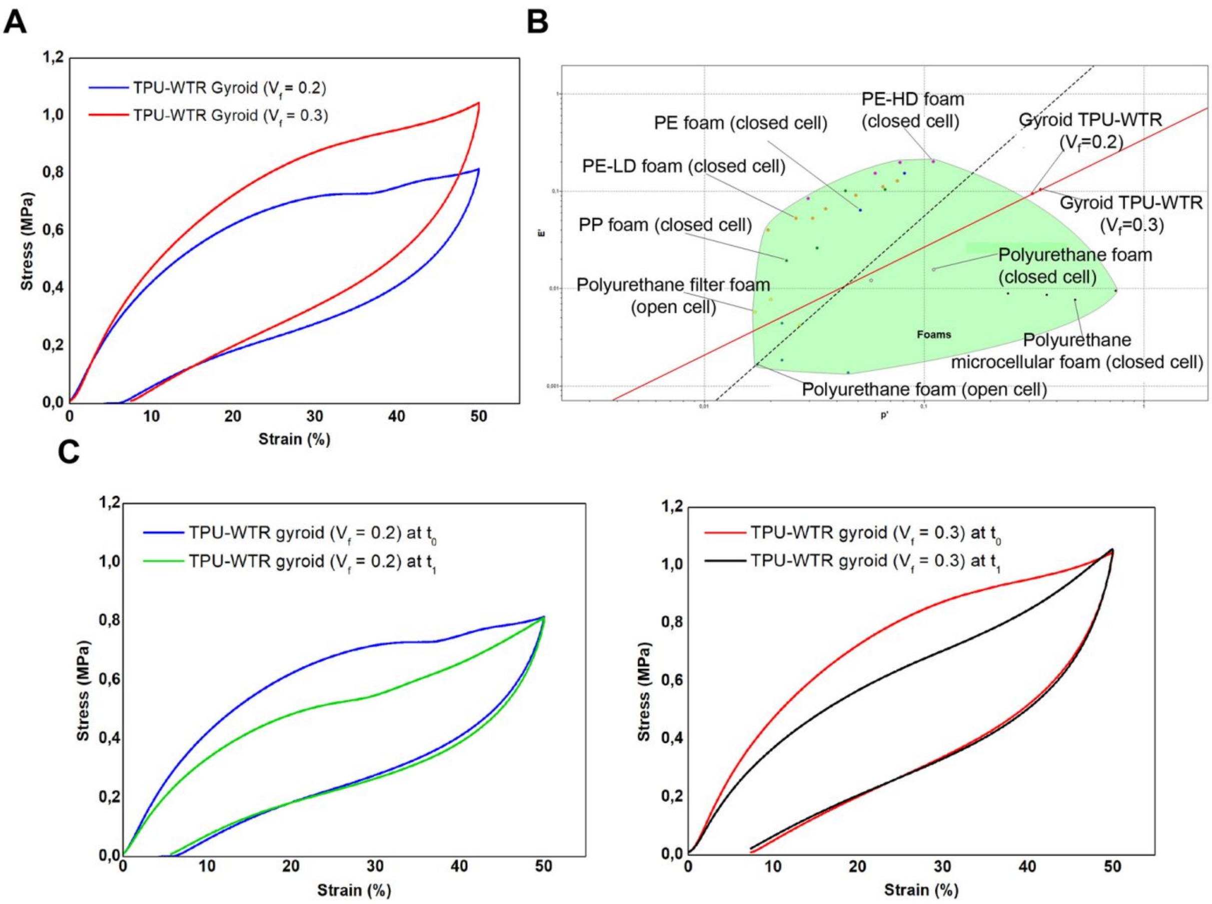

Figure 10. (A) Average stress-strain compression curves of 4 × 4 × 4 gyroid arrays with volume fractions of 0.2 and 0.3. (B) Relative compressive elastic modulus of the studied 4 × 4 × 4 gyroid lattices with volume fractions of 0.2 and 0.3 as a function of the relative density mappedtogether with data of different polyurethane foams. (C) Average stress-strain compression curves of 4 × 4 × 4 gyroid arrays with volume fractions of 0.2 and 0.3 before (t_0) and after a 20-minute rest period of relaxation (t_1).

Moreover, this highlights that the chemical composition of TPU-WTR does not affect the performance of 3D-printed gyroid structures.Furthermore, the gyroid lattice exhibits higher mechanical strengththan traditional polyurethane foams. The mean interpolation line of polyurethane foams has a steeper slope, characterised by n = 2, which signifies bending-dominated structures.

Lastly, it was observed that all 4 × 4 × 4 gyroid arrays tested exhibited a remarkable 98.6% shape recovery after a 20-minute rest period of relaxation, irrespective of the volume fraction. Consequently, the behaviour of the gyroid arrays under the same conditions was reanalysed.

Figure 10C depicts the average stress vs. strain curves at t_0, representing the first application of the stimulus at 0 minutes, and at t_1, indicating the subsequent force application after 20 minutes of relaxation. The initial notable difference between the two behaviours is the amount of absorbed energy, as evidenced by the area under the curve during the first compression, which consistently exceeds that of the second test. This outcome was expected, as a never-tested sample experiences a more significant loss of elasticity than a previously tested one, absorbing considerable energy through plastic deformation. However, intriguingly, it is worth noting that the arrays subjected to an initial compression (potentially exhibiting micro/nano fractures within the structure) managed to attain peak stress values similar to the samples tested at t_0 after the 20-minute relaxation period. This unique feature, previously unseen in gyroid lattice structures fabricated with TPU, may be attributed to the presence of the WTR particles. It holds a particular interest in applications involving shock absorption. However, further investigations are needed.

4. Conclusion

This study discusses the mechanical properties, printing parameters, and potential applications of an innovative TPU-based filament. This filament, labelled TPU-WTR, is obtained as a blend between a TPU matrix and Waste-Tire-Rubber particles (80/20 %wt). The contribution is thus twofold: 1) explore the potentials of a new AM filament for MEX; 2) provide informed examples of how AM processes, and particularly MEX, can contribute to the CEparadigm. An in-depth experimental campaign compared the new TPU-WTR filament with its virgin condition, i.e., aTPU filament.

Once the optimal printing parameters for the new material were identified, mechanical properties were derived through tensile tests, including Poisson's ratio. Besides, compressive tests were performed on TPMS-based lattices. Based on the results obtained, the presence of WTR improves the material's mechanical properties. Specifically, recycled tire particles in the TPU-WTR materials led to a significant increase of 114% compared to the virgin TPU. On the other hand, the hysteresis analysis demonstrated a 14% reduction in the percentage of elasticity for the TPU-WTR.

However, this improvement occurs if the blend between the TPU matrix and the WTR particles is appropriately performed. The lattice structures were successfully printed. Also, quasi-static compression tests and the hysteresis characterisation performed on the printed structures demonstrated that TPMS-based lattices printed with this material could be exploited for energy-absorbing applications. In particular, the 4 × 4 × 4 gyroid arrays made of TPU-WTR, with volume fractions of 0.2 and 0.3, revealed a Young's modulus of 5.57 ± 0.04 MPa and 6.11 ± 0.09 MPa, respectively. Both samples exhibited a 98.6% shape recovery following a 20-minute relaxation period. This unique feature, not observed in gyroid lattice structures previously fabricated with TPU, is likely attributed to the presence of WTR particles.

Hence, overall, the obtained results provide evidence of the importance of investing further efforts in strengthening the role of AM technologies and materials in CE to contribute to the SDGs and enlarge the availability of AM materials and, thus, the design opportunities they could offer.

Declaration of Competing Interest

The authors declare no competing interest.

Author Contributions: “Conceptualization, R.P. and S.G.; methodology, S.B., S.G., and R.P.; software,S.B., S.G., and R.P.; validation,S.B., S.G., and R.P.; formal analysis, S.B., S.G., M.E.R.M.C. and R.P.; investigation,S.B., S.G. and R.P.; data curation,S.G. and R.P.; writing—original draft preparation,R.P. and S.G.; writing—review and editing,S.B., S.R., S.G., M.E.R.M.C. and R.P.; visualization,S.G. and R.P.; supervision, R.P. and S.G.; project administration, R.P.; funding acquisition,S.G., S.R., and R.P.. All authors have read and agreed to the published version of the manuscript.”

Acknowledgments: We thank Treed Filaments for their provision of filaments and valuable discussions regarding printing properties. We also thank Sharebot for their technical support on the 3D printers. Besides, we thank Lorenzo Giudici and Mauro De Mori for their help with the mechanical testing setup.

References

Alessia Romani, Raffaella Suriano and Levi, M. (2023), "Biomass waste materials through extrusion-based additive manufacturing: A systematic literature review", *Journal of Cleaner Production,* Vol. 386.

Ali Fazli and Rodrigue, D. (2020), "Recycling Waste Tires into Ground Tire Rubber (GTR)/Rubber Compounds: A Review", *J. Compos. Sci.,* Vol. 4 No. 3.

Alkadi, F., Lee, J., Yeo, J.-S., Hwang, S.-H. and Choi, J.-W. (2019), "3D Printing of Ground Tire Rubber Composites", *Int. J. Precis. Eng. Manuf.,* Vol. 6 No. 2.

Antoniya Toncheva, Loïc Brison, Philippe Dubois and Laoutid, F. (2021), "Recycled Tire Rubber in Additive Manufacturing: Selective Laser Sintering for Polymer-Ground Rubber Composites", *applied sciences,* Vol. 11 No. 18.

Ashby, M. F. (2005), "The properties of foams and lattices", *Philosophical Transactions of the Royal Society A: Mathematical, Physical and Engineering Sciences,* Vol. 364 No. 1838.

Ashby, M. F. (2006), "The properties of foams and lattices", *Philosophical Transactions of the Royal Society A: Mathematical, Physical and Engineering Sciences,* Vol. 364.

Bahçegül, E. G., Bahçegül, E. and O¨zkan, N. (2020), "3D printing of hemicellulosic biopolymers extracted from lignocellulosic agricultural wastes", *ACS Appl. Polym. Mater.,* Vol. 2.

Biswas, M., Jeelani, S. and Rangari, V. (2017), "Influence of biobased silica/carbon hybrid nanoparticles on thermal and mechanical properties of biodegradable polymer films", *Compos. Commun.,* Vol. 4.

Can Jiang, Yousheng Zhang, Li Ma, Ling Zhou and He, H. (2018), "Tailoring the properties of ground tire rubber/high-density polyethylene blends by combining surface devulcanization and in-situ grafting technology", *Materials Chemistry and Physics,* Vol. 220 No. 1.

Coppola, B., Garofalo, E., Di Maio, L., Scarfato, P. and Incarnato, L. (1981), "Investigation on the use of PLA/hemp composites for the fused deposition modelling (FDM) 3D printing", *AIP Conf. Proc.,* Vol. 1.

Dániel Ábel Simon and Bárány, T. (2023), "Microwave Devulcanization of Ground Tire Rubber and Its Improved Utilization in Natural Rubber Compounds", *ACS Sustainable Chem. Eng.,* Vol. 11 No. 5.

David Downing , Alistair Jones , Milan Brandt and Leary, M. (2021), "Increased efficiency gyroid structures by tailored material distribution", *Materials & Design,* Vol. 197.

Faez Alkadi, Jeongwoo Lee, Jun-Seok Yeo, Seok-Ho Hwang and Choi, J.-W. (2019), "3D Printing of Ground Tire Rubber Composites", *International Journal of Precision Engineering and Manufacturing-Green Technology* Vol. 6.

Ferrao, P., Ribeiro, P. and Silva, P. (2008), "A management system for end-of-life tyres: a Portuguese case study", *Waste Manag,* Vol. 28 No. 3, pp. 604-14.

Fico, D., Rizzo, D., Casciaro, R. and Esposito Corcione, C. (2022), "A Review of Polymer-Based Materials for Fused Filament Fabrication (FFF): Focus on Sustainability and Recycled Materials", *Polymers (Basel),* Vol. 14 No. 3.

Filgueira, D., Holmen, S., Melbø, J., Moldes, D., Echtermeyer, A. and Chinga-Carrasco, G. (2018), "3D printable filaments made of biobased polyethylene biocomposites.", *Polymers (Basel),* Vol. 10 No. 314.

Gama, N., Magina, S., Barros-Timmons, A. and Ferreira, A. (2021), "Enhanced compatibility between coconut fibers/PP via chemical modification for 3D printing", *Progress in Additive Manufacturing volume,* Vol. 7.

Gonzalo Martínez-Barrera, Juan José del Coz-Díaz, Felipe Pedro Álvarez-Rabanal, Fernando López Gayarre, Miguel Martínez-López and Cruz-Olivares, J. (2020), "Waste tire rubber particles modified by gamma radiation and their use as modifiers of concrete", *Case Studies in Construction Materials,* Vol. 12.

Helge Schneevogt, Kevin Stelzner, Buket Yilmaz, Bilen Emek Abali, Andre Klunker and Vollmecke, C. (2021), "Sustainability in additive manufacturing: Exploring the mechanical potential of recycled PET filaments", *Composites and Advanced Materials,* Vol. 30 No. 1.

Hieu Tri Nguyen, Kelly Crittenden, Leland Weiss and Bardaweel, H. (2022), "Recycle of waste tire rubber in a 3D printed composite with enhanced damping properties", *Journal of Cleaner Production,* Vol. 368 No. 25.

Huan Liang, Jacob Dion Gagné, Adrien Faye, Denis Rodrigue and Brisson, J. (2020), "Ground tire rubber (GTR) surface modification using thiol-ene click reaction: Polystyrene grafting to modify a GTR/polystyrene (PS) blend", *Progress in Rubber, Plastics and Recycling Technology,* Vol. 36 No. 2.

Hussien Hega, Navneet Khanna, Neamat Monib and Salem, A. (2023), "Design for sustainable additive manufacturing: A review", *Sustainable Materials and Technologies,* Vol. 35.

I. Maskery, A.O. Aremu, L. Parry, R.D. Wildman, C.J. Tuck and Ashcroft, I. A. (2018a), "Effective design and simulation of surface-based lattice structures featuring volume fraction and cell type grading", *Materials & Design,* Vol. 155.

I. Maskery, L. Sturm, A.O. Aremu, A. Panesar, C.B. Williams, C.J. Tuck, R.D. Wildman, I.A. Ashcroft and Hague, R. J. M. (2018b), "Insights into the mechanical properties of several triply periodic minimal surface lattice structures made by polymer additive manufacturing", *Polymer,* Vol. 152.

I. Maskery, L.A. Parry, D. Padrão, R.J.M. Hague and Ashcroft, I. A. (2022), "FLatt Pack: A research-focussed lattice design program", *Additive Manufacturing,* Vol. 49.

Jafar Ghorbani, Pratik Koirala, Yu-Lin Shen and Tehrani, M. (2022), "Eliminating voids and reducing mechanical anisotropy in fused filament fabrication parts by adjusting the filament extrusion rate", *Journal of Manufacturing Processes,* Vol. 80.

Jagoda Worek, Xymena Badura, Anna Białas, Joanna Chwiej, Kamil Kawoń and Styszko, K. (2022), "Pollution from Transport: Detection of Tyre Particles in Environmental Samples", *energies,* Vol. 15 No. 8.

János Plocher and Panesar, A. (2020), "Effect of density and unit cell size grading on the stiffness and energy absorption of short fibre-reinforced functionally graded lattice structures", *Additive Manufacturing,* Vol. 33.

Javier Araujo-Morera, Raquel Verdejo, Miguel Angel López-Manchado and Santana, M. H. n. (2021), "Sustainable mobility: The route of tires through the circular economy model", *Waste Management,* Vol. 126 No. 3.

Jiawei Feng, Jianzhong Fu, Xinhua Yao and He, Y. (2022), "Triply periodic minimal surface (TPMS) porous structures: from multi-scale design, precise additive manufacturing to multidisciplinary applications", *International Journal of Extreme Manufacturing,* Vol. 4 No. 2.

K. Monkova, P. Monka, I. Zetková, P. Hanžl and Manduľák, D. (2017), "Three Approaches to the Gyroid Structure Modelling as a Base of Lightweight Component Produced by Additive Technology", *DEStech Transactions on Computer Science and Engineering,* Vol. 1.

Kosciuszko, A., Sykutera, D., Czyzewski, P., Hoyer, S., Kroll, L. and Szczupak, B. (2022), "Processing and Mechanical Properties of Highly Filled PP/GTR Compounds", *Materials (Basel),* Vol. 15 No. 11.

Laoutid, F., Lafqir, S., Toncheva, A. and Dubois, P. (2021), "Valorization of Recycled Tire Rubber for 3D Printing of ABS- and TPO-Based Composites", *Materials (Basel),* Vol. 14 No. 19.

Lu Liu, Yongqiang Wu and Zhu, Z. (2017), "Internal structure and crystallinity investigation of segmented thermoplastic polyurethane elastomer degradation in supercritical methanol", *Polymer Degradation and Stability,* Vol. 140.

Paulina Wiśniewska, Natalia A. Wójcik, Jacek Ryl, Robert Bogdanowicz, Henri Vahabi, Krzysztof Formela and Saeb, M. R. (2023), "Rubber wastes recycling for developing advanced polymer composites: A warm handshake with sustainability", *Journal of Cleaner Production,* Vol. 427 No. 15.

Pringle, A. M., Rudnicki, M. and Pearce, J. M. (2018), "Wood furniture waste–based recycled 3-D printing filament.", *For. Prod. J.,* Vol. 68.

Pugliese, R. and Graziosi, S. (2023), "Biomimetic scaffolds using triply periodic minimal surface-based porous structures for biomedical applications", *SLAS Technol,* Vol. 28 No. 3, pp. 165-182.

Riccardo Sala, Stefano Regondi, Serena Graziosi and Pugliese, R. (2022), "Insights into the printing parameters and characterization of thermoplastic polyurethane soft triply periodic minimal surface and honeycomb lattices for broadening material extrusion applicability", *Additive Manufacturing,* Vol. 58.

S. Ramarad, M. Khalid, C.T. Ratnam, A. Luqman Chuah and Rashmi, W. (2015), "Waste tire rubber in polymer blends: A review on the evolution, properties and future", *Progress in Materials Science,* Vol. 72.

Sauerwein, M. and Doubrovski, E. L. (2018), "Local and recyclable materials for additive manufacturing: 3D printing with mussel shells", *Today Commun.,* Vol. 15.

Sienkiewicz, M., Kucinska-Lipka, J., Janik, H. and Balas, A. (2012), "Progress in used tyres management in the European Union: a review", *Waste Manag,* Vol. 32 No. 10, pp. 1742-51.

Sigmund A. Tronvoll, Torgeir Welo and Elverum, C. W. (2018), "The effects of voids on structural properties of fused deposition modelled parts: a probabilistic approach", *The International Journal of Advanced Manufacturing Technology,* Vol. 97.

Stavros Ponis, Eleni Aretoulaki, Theodoros Nikolaos Maroutas, George Plakas and Dimogiorgi, K. (2021), "A Systematic Literature Review on Additive Manufacturing in the Context of Circular Economy", *Sustainability,* Vol. 13 No. 11.

Suganti Ramarad, Chantara Thevy Ratnam, Mohammad Khalid and Chuah, A. L. (2015), "Improving the properties of reclaimed waste tire rubber by blending with poly(ethylene-co-vinyl acetate) and electron beam irradiation", *Journal of applied polymer science,* Vol. 132 No. 11.

Takeshi Amari, Nickolas J Themelis and Wernick, I. K. (1999), "Resource recovery from used rubber tires", *Resources Policy,* Vol. 25 No. 3.

Tyler DeValk and Lakes, R. (2021), "Poisson's Ratio and Modulus of Gyroid Lattices", *physica status solidi B,* Vol. 258.

Wang, Z., Fang, Z., Xie, Z. and Smith, D. E. (2022), "A Review on Microstructural Formations of Discontinuous Fiber-Reinforced Polymer Composites Prepared via Material Extrusion Additive Manufacturing: Fiber Orientation, Fiber Attrition, and Micro-Voids Distribution", *Polymers (Basel),* Vol. 14 No. 22.

Yan, C., Hao, L., Hussein, A. and Young, P. (2015), "Ti-6Al-4V triply periodic minimal surface structures for bone implants fabricated via selective laser melting", *J Mech Behav Biomed Mater,* Vol. 51, pp. 61-73.

Yubo Tao, Fangong Kong, Zelong Li, Jingfa Zhang, Xin Zhao, Qing Yin, Dan Xing and Li, P. (2021), "A review on voids of 3D printed parts by fused filament fabrication", *Journal of Materials Research and Technology,* Vol. 15.

Zahir Ahmed Khan and Faizan, M. (2023), "Mixing strategy and tensile strength characterization of WTR-PP composite", *International Journal of Polymer Analysis and Characterization* Vol. 28 No. 5.

Zedler, L., Burger, P., Wang, S. and Formela, K. (2020), "Ground Tire Rubber Modified by Ethylene-Vinyl Acetate Copolymer: Processing, Physico-Mechanical Properties, Volatile Organic Compounds Emission and Recycling Possibility", *Materials (Basel),* Vol. 13 No. 20.

CREDIT LINE FOR FIGURE AND TABLE

Source: Figure and table by authors

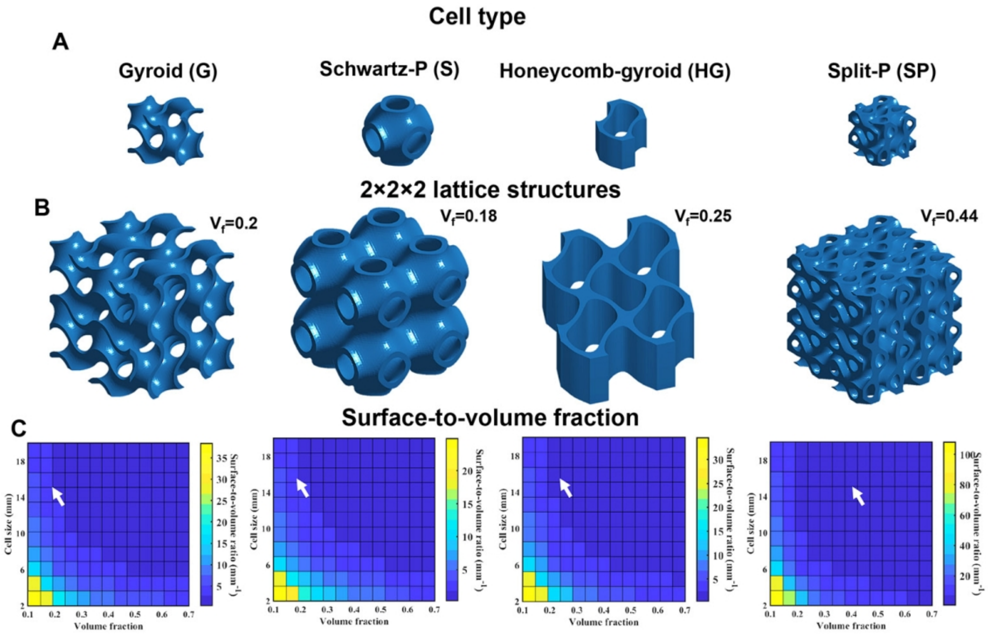

Figure 1. (A) Unit cell geometry of gyroid (G), schwartz-P (S), honeycomb-gyroid (HG), split-P (SP), and (B) corresponding to 2×2×2 lattice with different volume fraction (Vf). (C) The surface-to-volume ratio for each tested lattice was determined using the FLatt Pack "surface-to-volume estimation" feature.

130x82mm (300 x 300 DPI)

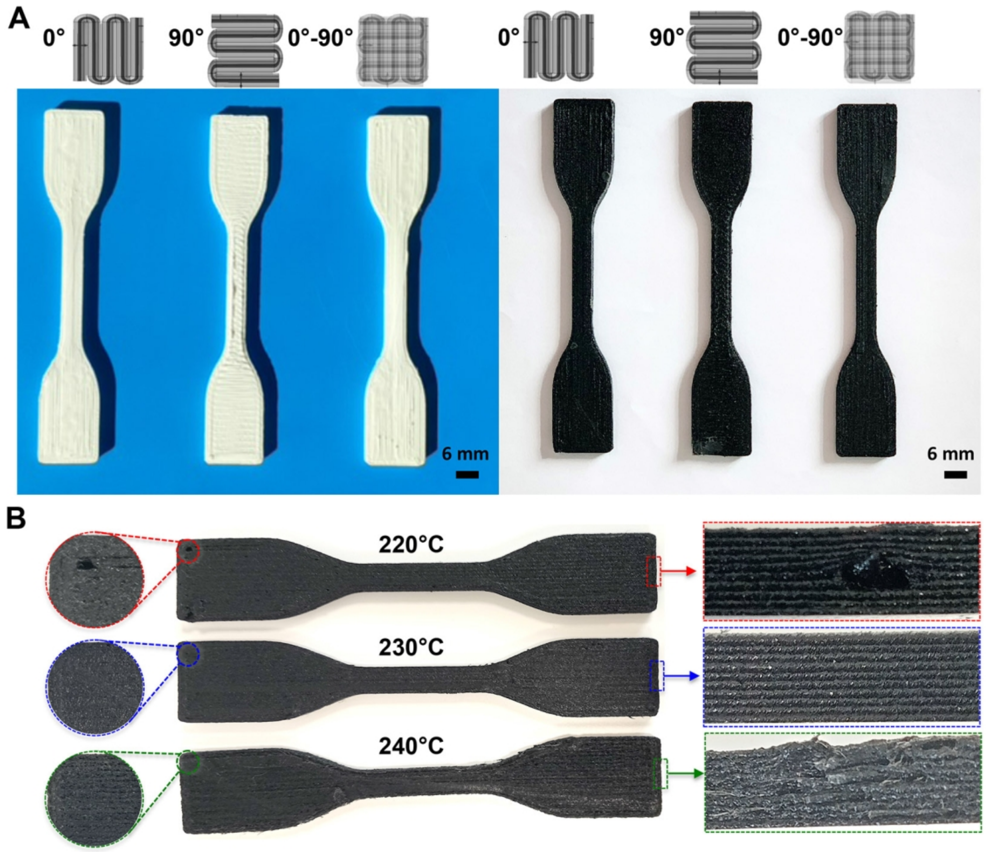

Caption : Figure 2. (A) ASTM D638-14 type IV dogbone specimens of TPU (on the left) and TPU-WTR (on the right) printed at three different raster angles (0°, 90°, 0-90°). (B) Detailed comparison of printing quality achieved with the three nozzle temperatures of 220, 230, and 240 °C. The sample printed at 230°C shows high quality and definition without any visible defects, whereas samples printed at 220°C and 240°C exhibit holes, voids, and overheating issues, indicating a lack of material homogeneity and decreased interlayer adhesion.

139x119mm (300 x 300 DPI)

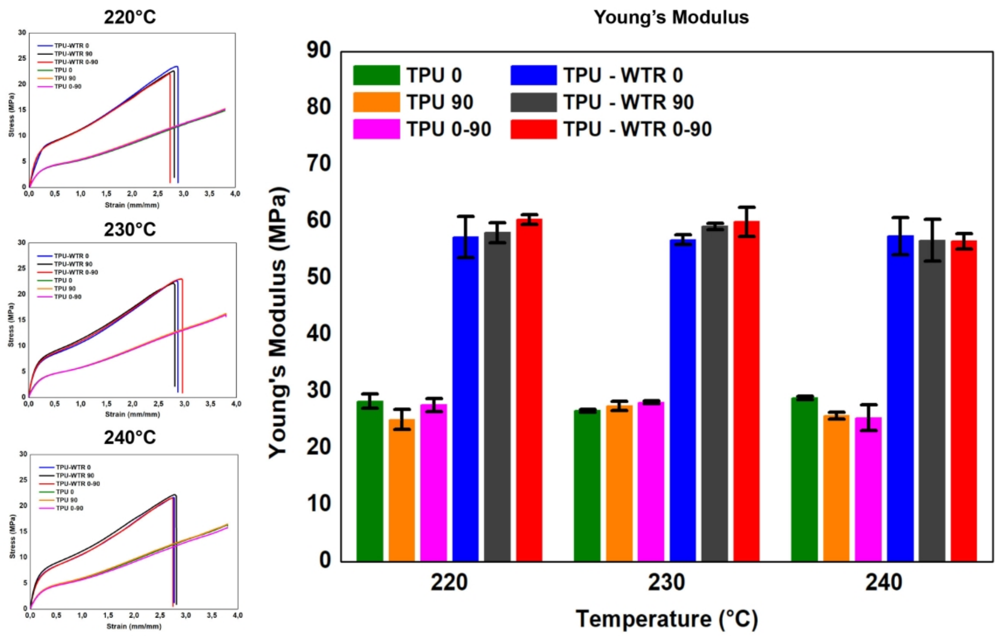

Figure 3. Effect of raster angles (0°, 90°, and 0°-90°) and printing temperature (220°C, 230°C, and 240°C) under tensile loading for TPU and TPU-WTR samples. All samples showed an isotropic-like mechanical behaviour along printing directions. However, recycled tire particles in TPU-WTR significantly increased its tensile behaviour compared to wild-type TPU.

223x143mm (300 x 300 DPI)

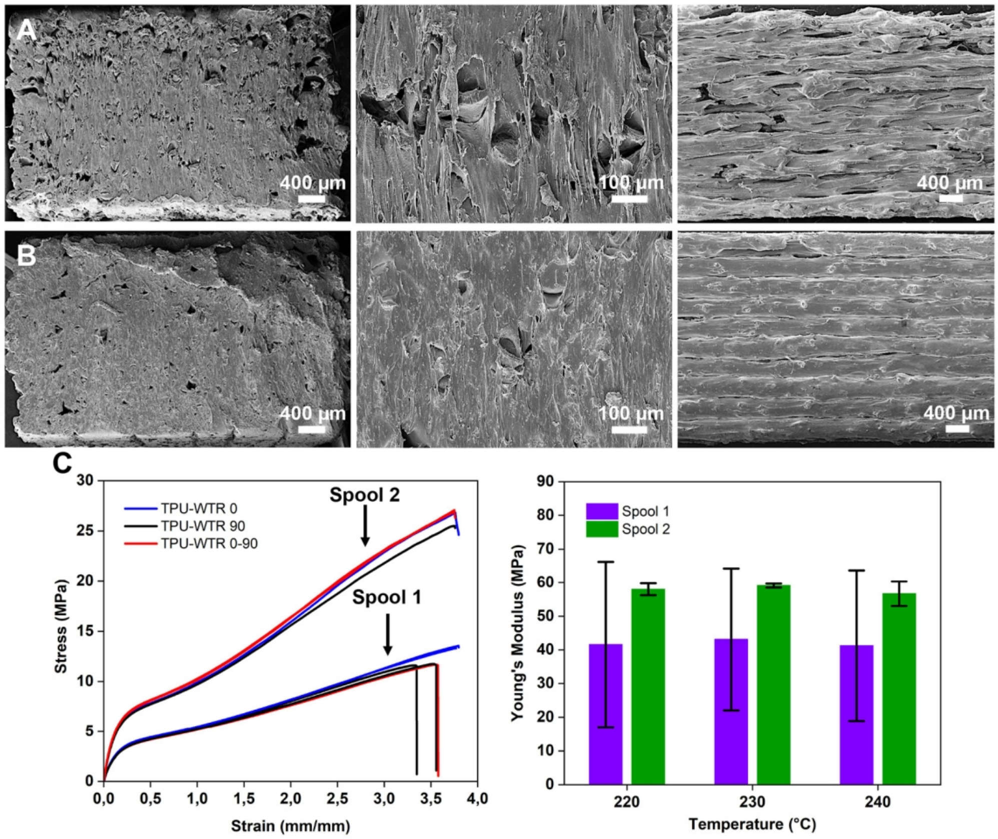

Figure 4. SEM analysis of (A) TPU-WTR dogbone made from an incorrect tire-elastomer compound and (B) adequately casted TPU-WTR filament. The incorrect compound formation resulted in poor appearance and low interlayer adhesion of the final printed dogbone, while the properly casted filament provided a high-quality printed dogbone with no visible defects. (C) Comparison between the Young's Modula obtained with dogbones printed with an incorrect (spool 1, in purple) and a correct (spool 2, in green) TPU-WTR compound under tensile loading.

142x119mm (300 x 300 DPI)

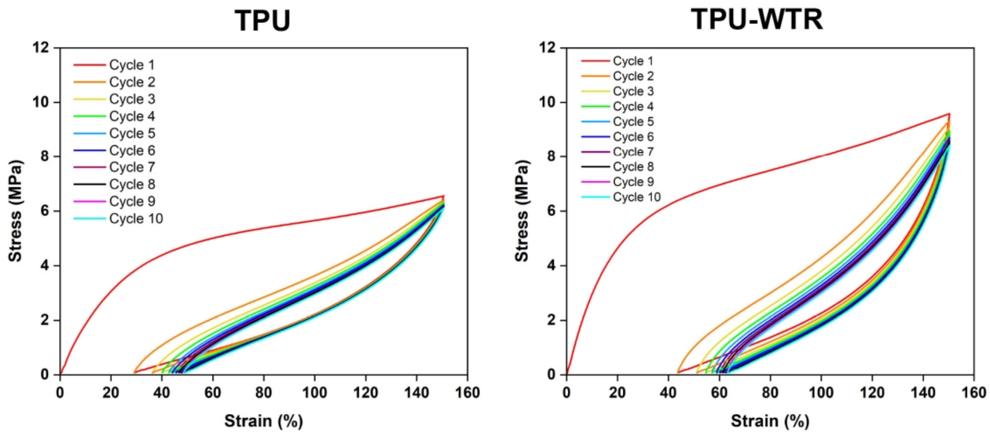

Figure 5. Hysteresis curves with mean values of TPU and TPU-WTR samples.

170x76mm (300 x 300 DPI)

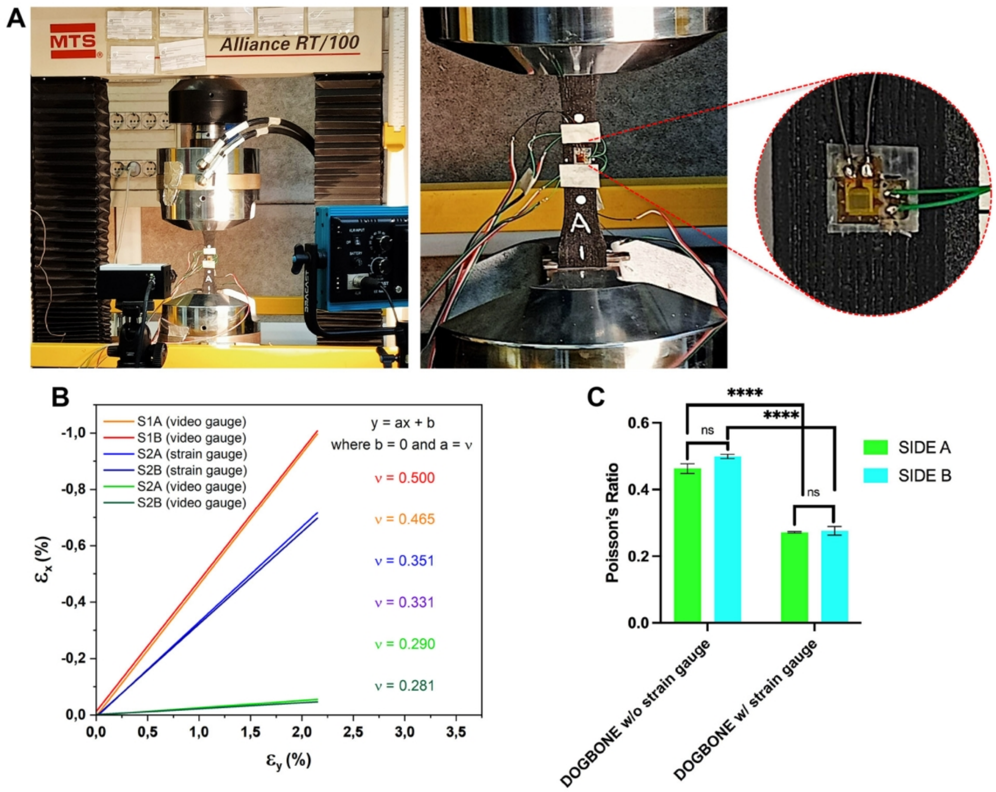

Figure 6. (A) The testing set-up for Poisson's ratios assessment showing a bi-axial strain gauge MM-F003109 in combination with a video gauges ProViSys VideoTraction. On the right, the magnification of ASTM D638-14 dogbone type III shows the strain gauge connected to the sample by cyanoacrylate adhesive (B) Graph of εy vs. εx of tested TPU-WTR samples. The slope of each curve identifies Poisson's ratios. S1 and S2 stand for sample 1 and sample 2, respectively, while letters A and B define the dogbone's bottom and top layers. (C) Statistical analysis on the Poisson's ratio of the samples with and without strain gauges. There is no statistically significant difference between the two sides of the same sample (labelled with ns = "not-significant"). Instead, a statistically significant difference (****p<0.0001) between the same faces of the two considered samples was found, ascribable to the cyanoacrylate adhesive used for strain gauge installation, which affects the test locally along the x direction, thus increasing the sample's stiffness and reducing Poisson's ratio.

163x129mm (300 x 300 DPI)

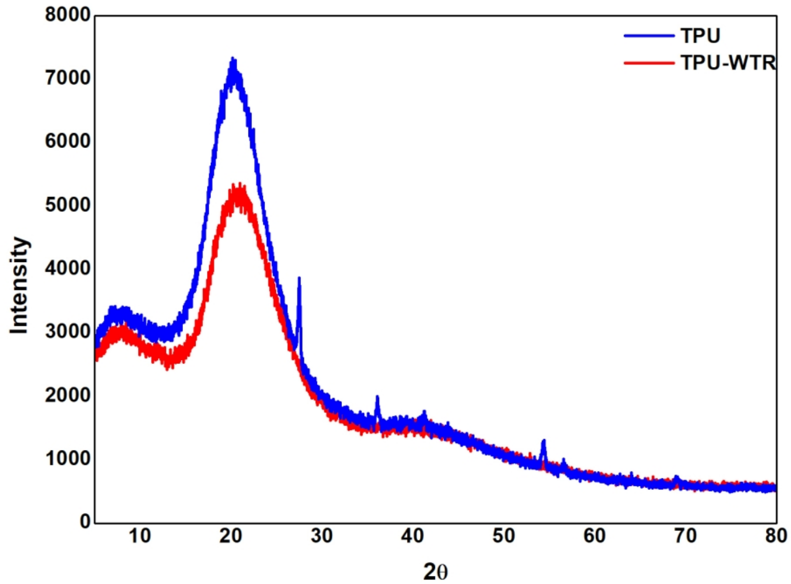

Figure 7. The XRD patterns of the TPU (blue line) and TPU-WTR (red line) to discrete reflections at appropriate 2θ values.

297x209mm (150 x 150 DPI)

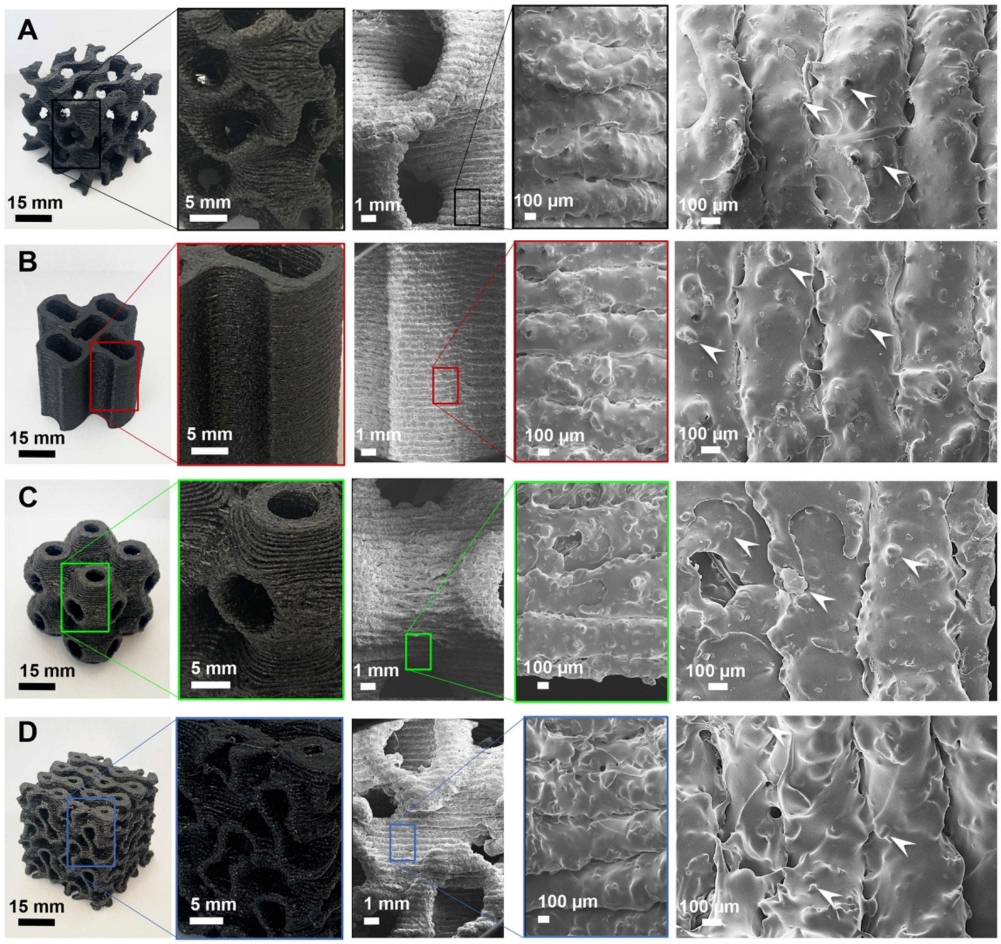

Figure 8. SEM images of the TPU-WTR-based lattice structures: (A) Gyroid, (B) Schwartz-P, (C) Honeycomb-gyroid, and (D) Split-P. The magnification of the surface (in black, red, light green, and blue) shows the printing quality of all recycled lattices. In the magnification on the right, the arrows indicate tire rubber micro-particles.

147x140mm (300 x 300 DPI)

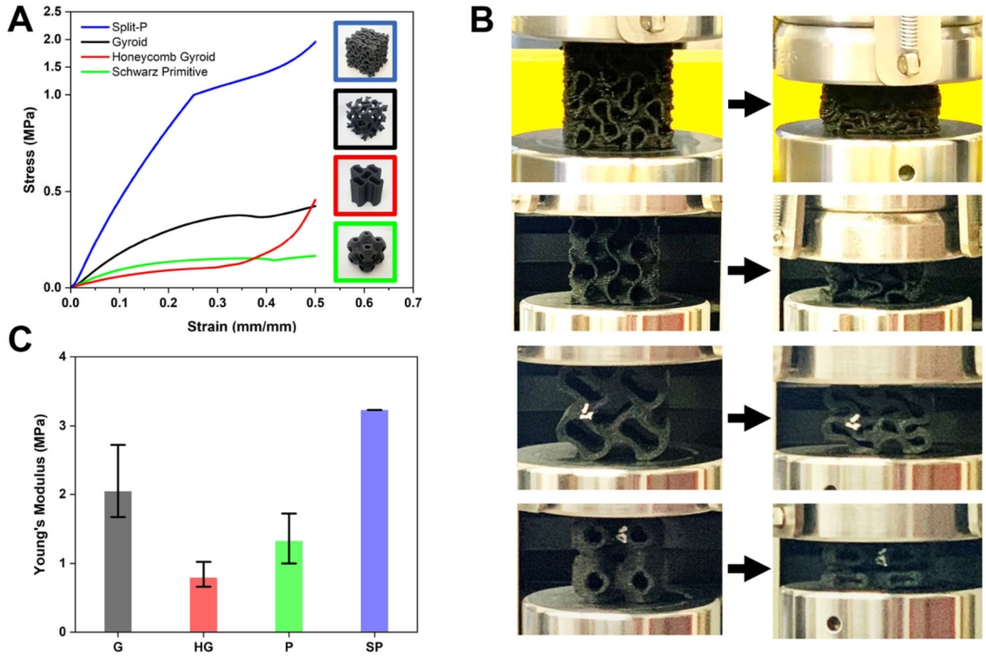

Figure 9. Quasi-static compression tests of 3D-printed TPMS structures. (A) The stress-strain response of TPMS samples. (B) SP, G, P, and HG densification after peak stress. (C) Average Young's modulus of all tested cell topologies, with SP having the highest modulus and HG having the lowest. Note that the obtained data cannot be strictly compared due to the different relative densities of the lattice structures.

147x99mm (300 x 300 DPI)

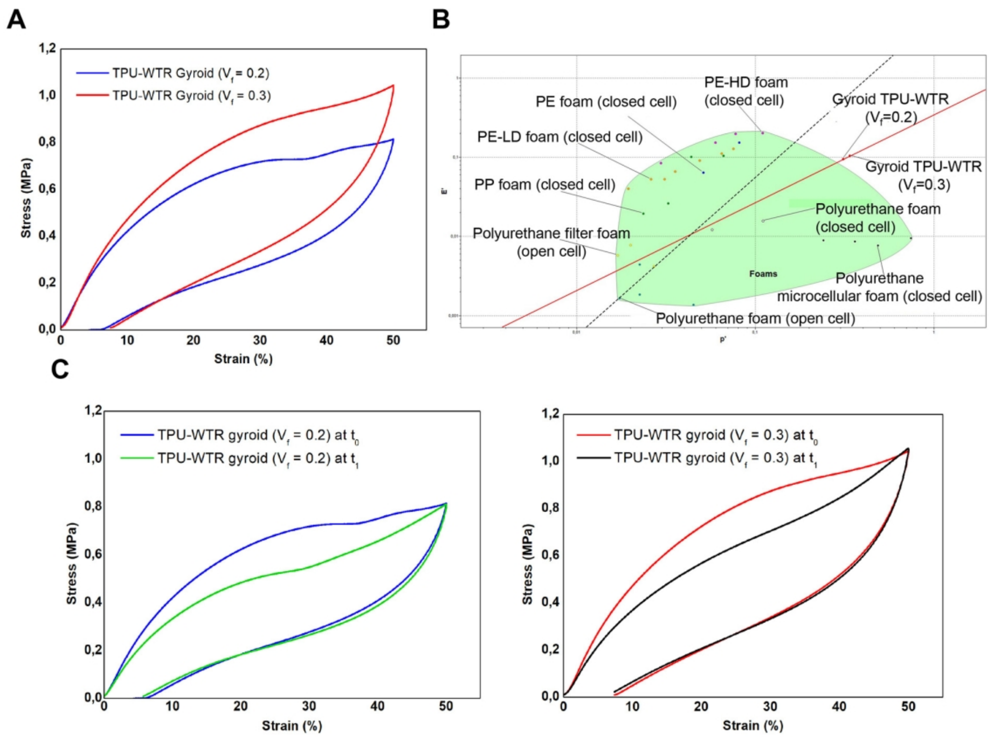

Figure 10. (A) Average stress-strain compression curves of 4 × 4 × 4 gyroid arrays with volume fractions of 0.2 and 0.3. (B) Relative compressive elastic modulus of the studied 4 × 4 × 4 gyroid lattices with volume fractions of 0.2 and 0.3 as a function of the relative density mapped together with data of different polyurethane foams. (C) Average stress-strain compression curves of 4 × 4 × 4 gyroid arrays with volume fractions of 0.2 and 0.3 before (t0) and after a 20-minute rest period of relaxation (t1).

162x119mm (300 x 300 DPI)

	Raster angle	Temperature (°C)		
		220	**230**	**240**
E_{TPU} (MPa)	0°	28.30 ± 1.30	26.63 ± 1.74	28.87 ± 1.17
	90°	25.07 ± 0.25	26.63 ± 1.74	25.73 ± 0.25
	0°-90°	27.60 ± 0.27	28.10 ± 0.61	25.37 ± 2.25
$E_{TPU-WTR}$ (MPa)	0°	57.23 ± 3.62	56.76 ± 0.85	57.44 ± 3.27
	90°	58.02 ± 1.78	59.13 ± 0.59	56.70 ± 3.68
	0°-90°	60.37 ± 0.88	59.96 ± 2.59	56.50 ± 1.37

S1A (video gauge)		S2A (video gauge)		S2A (strain gauge)	
εx (%)	εy (%)	εx (%)	εy (%)	εx (%)	εy (%)
- 0.2	0.45	- 0.11	0.41	- 0.1	0.31
S1B (video gauge)		**S2B (video gauge)**		**S2B (strain gauge)**	
εx (%)	εy (%)	εx (%)	εy (%)	εx (%)	εy (%)
- 0.19	0.38	- 0.1	0.38	- 0.14	0.36

Supplementary information for

Sustainable 3D printing with recycled tire rubber-based filaments: an investigation of process parameters and mechanical behaviour

Table of Content

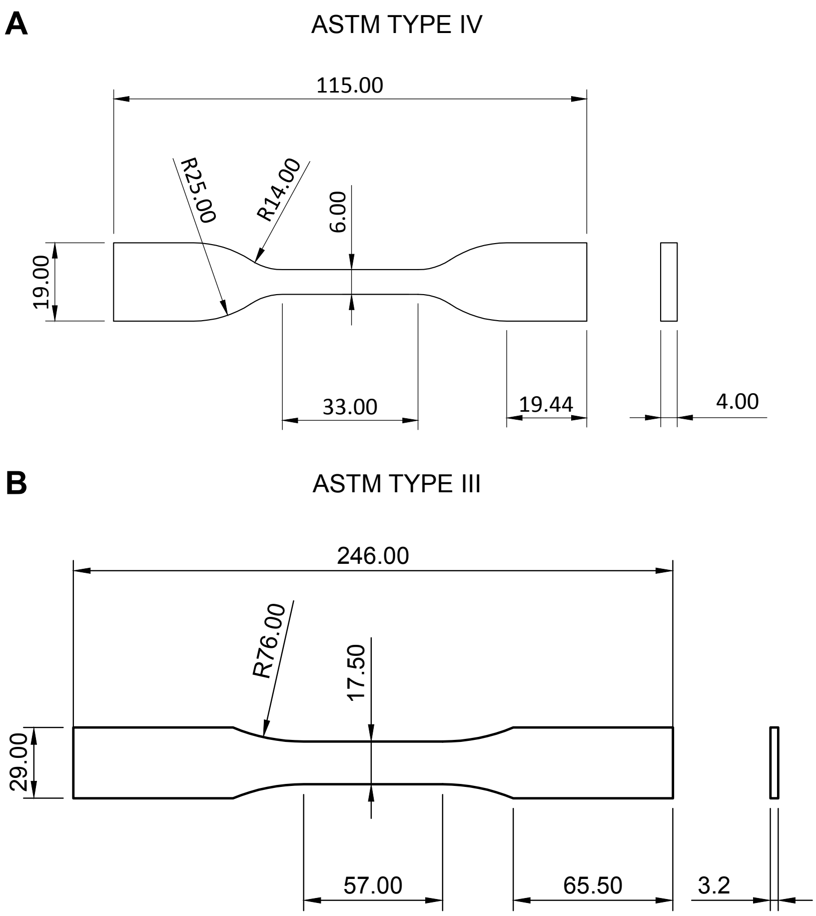

Figure S1. Geometry and dimensions of the dogbone samples ASTM D638-14 type IV and III.

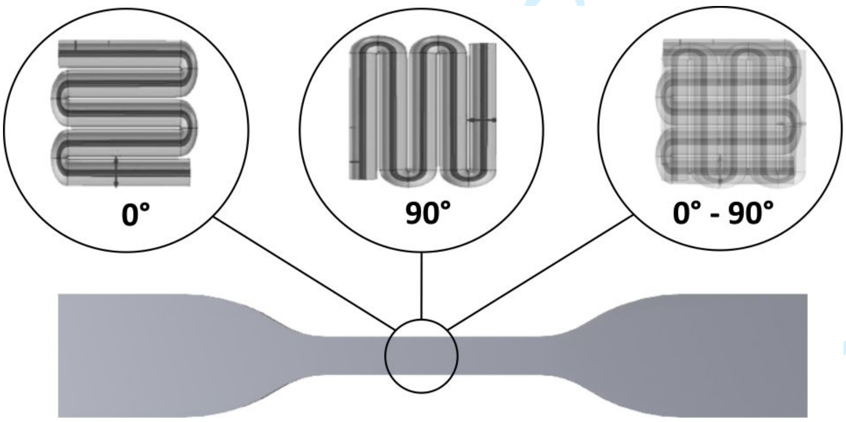

Figure S2. The three printing orientations selected for the ASTM D638-14 type IV sample.

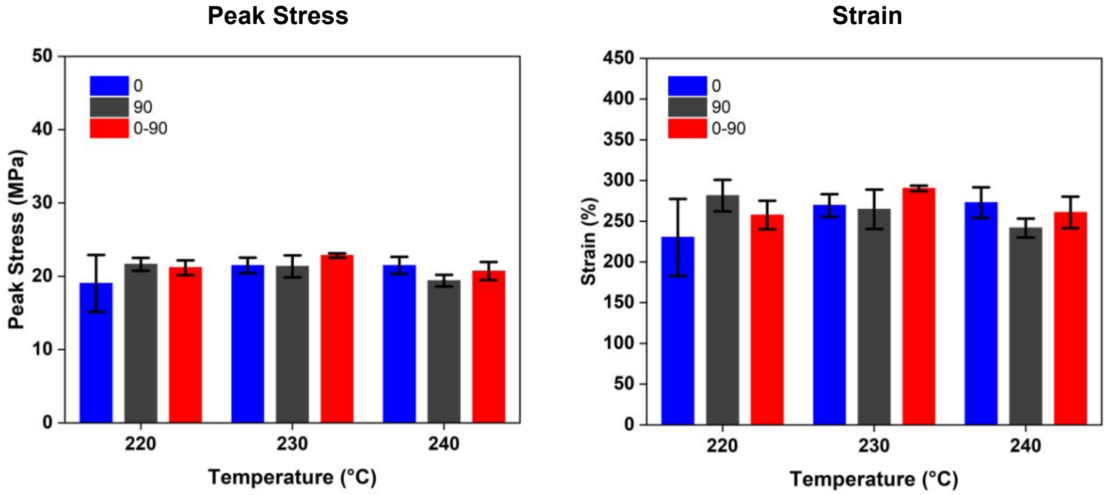

Figure S3. Peak stress and strain at breakage of TPU-WTR with different raster angles and printing temperature.

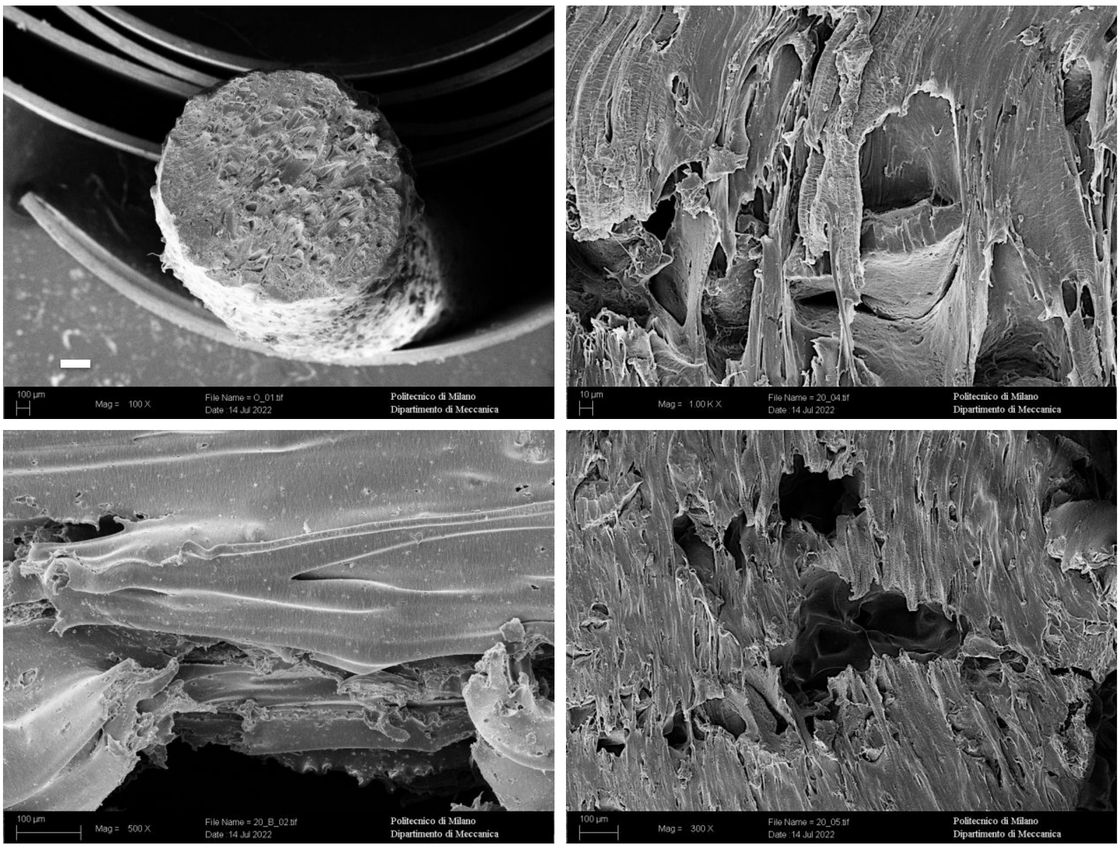

Figure S4. SEM analysis of TPU-WTR filament made from an incorrect tire-elastomer compound.

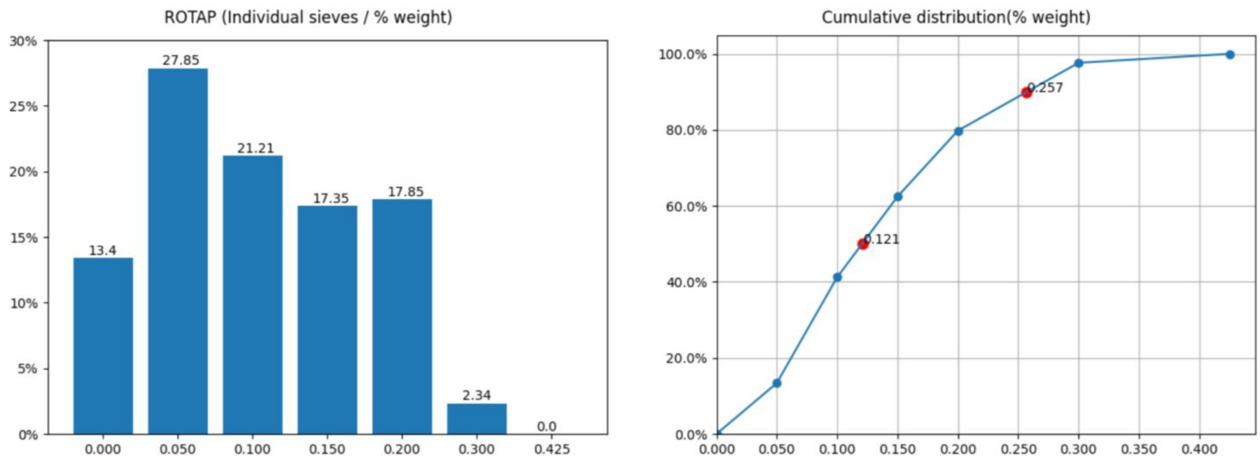

Figure S5. Granulometric distribution of recycled tire particles and cumulative distribution granulometric curve of TPU-WTR compound.

Type of filament	Nozzle diameter (mm)	Extrusion multiplier (-)	Extrusion width (mm)	Platform temperature (°C)	Fan speed (%)	Printing speed (mm/min)	Outline underspeed (%)	Outline overlap (%)	Extruder retraction distance (mm)	Extra restart distance (mm)	Coasting distance (mm)	Wipe distance (mm)	Retraction vertical lift (mm)
TPU	0.8	1.1	0.9	60	20	1500	75	70	0	2	0.5	3	0
TPU-WTR	0.8	1.0	0.96	60	0	1000	75	75	0.5	0	2.5	5	1

Table S1. Optimized printing parameters for TPU and TPU-WTR.

Sample n.	*Strain (%) TPU 1st cycle*	*Strain (%) TPU-WTR 1st cycle*	*Strain (%) TPU 10th cycle*	*Strain (%) TPU-WTR 10th cycle*
1	27.44	43.43	51.23	66.76
2	29.12	44.09	49.35	64.18
3	29.64	43.63	50.06	63.96
Average	28.73	43.72	50.21	64.96
Standard deviation	± 1.15	± 0.34	± 0.95	± 1.56

Table S2. Strain values of TPU and TPU-WTR at 1st and 10th hysteresis cycle.

	G	*P*	*HG*	*SP*
Extrusion Multiplier (-)	1.1	1.1	1.1	1.1
Extrusion width (mm)	0.9	0.9	0.9	0.9
Extrusion Temperature (°C)	220	220	220	215
Platform Temperature (°C)	60	60	60	60
Fan speed (%)	20	20	20	20
Printing speed (mm/min)	1500	1500	1500	1500
Speed reduction (%)	50	50	50	50
Outline underspeed (%)	75	75	75	75
Outline overlap (%)	70	70	70	70
Retraction distance (mm)	0	0	0	0
Extra restart distance (mm)	2	2	2	2
Wipe distance (mm)	5	5	5	5
Coasting distance (mm)	2	2	2	1
Thin wall type	Internal: perimeters only	Internal: perimeters only	Internal: perimeters only	Internal: perimeters only

Table S3. Optimized printing parameters for gyroid (G), schwartz-P (P), honeycomb-gyroid (HG), and Split-P (SP) made of TPU-WTR.